

Numerical modeling of heat transfer and fluid
flow in welding with a moving heat source

BSc Thesis

April 28, 2014

Author:
J.P.A. Beekers

Supervisors:
Ir. A. Kidess
Prof. dr. ir. C. R. Kleijn

Delft University of Technology
Faculty of Applied Sciences
Department of Transport Phenomena

Abstract

Worldwide, welding is a multi billion-dollar fabrication technology used extensively in construction and industry. The final quality of a weld is known to be dependent on the hydrodynamics in the liquid region and the energy transfer in the surrounding heat affected zone. Understanding of these processes is therefore vital in improving weld quality.

Within the department carrying out this project (Transport Phenomena), an OpenFOAM Solver has been developed for the simulation of welding with a stagnant heat source. A large part of welds in industrial application is performed with a moving heat source, integrating this motion into the existing solver is the goal of this thesis. In order to minimize the necessary grid size for simulation, and thereby reduce the computational load, the governing equations are formulated in a reference frame attached to the moving heat source.

First a detailed theoretical analysis is presented of heat transfer, phase change and fluid flow in welding of non pure material. Special attention is given to the modeling of the flow in the solid-liquid region and the modeling of thermocapillary surface forces which occur from spatial temperature differences. We assume no deformation of the weld pool surface and incorporate the thermocapillary surface forces and the heat flux through the top surface as boundary conditions.

The derived governing equations have been implemented in the existing OpenFOAM solver. A special feature of this solver is the linearization of the energy source term associated with the latent heat absorption and release due to the phase change.

Results generated by the modified solver are compared with analytical solutions of heat transfer. Finally temperature and velocity field data are presented for three different welding velocities and three different surface tension coefficients.

Contents

1	Introduction	5
1.1	Weld pool simulation	5
1.2	Research goal	5
1.3	Outline	6
2	Physical model	7
2.1	Physical phenomena in a weld pool	7
2.2	Heat transfer	8
2.2.1	Energy equation	8
2.2.2	Modeling of the phase change	9
2.2.3	Heat influx on the surface	9
2.2.4	Heat outflux on the surface	10
2.3	Fluid flow	11
2.3.1	Continuity- and momentum equation	11
2.3.2	Modeling of flow in the mushy zone	11
2.3.3	Modeling of the surface forces	11
2.4	Moving frame of reference	12
3	Numerical implementation	14
3.1	Finite Volume Method	14
3.1.1	Spatial discretization	14
3.1.2	Time integration	15
3.2	Mesh	15
3.3	Boundary conditions	17
3.4	Solver details	17
3.4.1	Splitting the energy source term	18
3.4.2	Computation sequence	18
4	Validation	20
4.1	Validation of thermal conduction	20
4.1.1	Stationary heat source	20
4.1.2	Moving heat source	22
4.2	Validation of convective heat flow	23
4.2.1	Stationary heat source	23
4.2.2	Moving heat source	25
4.3	Welding simulations with a moving heat source and fluid flow	26

5	Closure	38
5.1	General conclusions	38
5.2	Recommendations for future work	38
5.2.1	Free surface deformation	38
5.2.2	Mesh refinement	39
5.2.3	Investigation of the symmetry breaking cases	39
6	Appendix	42
6.1	Derivations for the change of reference frame	42
6.1.1	Continuity equation	42
6.1.2	Heat equation	42
6.1.3	Momentum equation	43
6.1.4	Overview of the validation cases of subsection 4.3	44

List of Symbols

α	Thermal diffusion coefficient	$[m^2s^{-1}]$
β	Thermal expansion coefficient	$[K^{-1}]$
ϵ	Emissivity	$[-]$
λ	Thermal conductivity	$[Wm^{-1}K^{-1}]$
μ	Dynamic viscosity	$[kgm^{-1}s^{-1}]$
ν	Kinematic viscosity	$[m^2s^{-1}]$
ρ	Density	$[kgm^{-3}]$
σ	Surface tension coefficient, Stefan-Boltzmann constant	$[Nm^{-1}]$, $[Wm^{-2}K^{-4}]$
c_p	Heat capacity	$[Jkg^{-1}K^{-1}]$
g	Liquid fraction, gravitational acceleration	$[-]$, $[ms^{-2}]$
H	Enthalpy	$[J]$
h_{gf}	Heat of evaporation	$[Jkg^{-1}]$
k_q	Laser beam distribution coefficient	$[-]$
L	Length, Latent heat	$[m]$, $[Jkg^{-1}K^{-1}]$
p	Pressure	$[kgm^{-1}s^{-2}]$
P	Laser power	$[W]$
r	Radius	$[m]$
r_q	Laser beam waist radius	$[m]$
T	Temperature	$[K]$
\vec{U}	Convective velocity	$[ms^{-1}]$
\vec{U}_t	Welding velocity of the laser	$[ms^{-1}]$
\vec{V}	Net velocity	$[ms^{-1}]$
W	Evaporation mass flux	$[kgm^{-2}s^{-1}]$

Subscripts s and l correspond to solid and liquid phase.

1 Introduction

1.1 Weld pool simulation

“In the last 20 years, the growth of modern welding science and technology has been phenomenal. Worldwide, welding is a multi billion-dollar fabrication technology used extensively in the construction of buildings and bridges and in the automotive, aircraft, aerospace, energy, ship build and electronic industries. Perhaps because welding is a construction technique, it is viewed by many as a primitive science. Nothing could be further from the truth”[4].

The final quality of a weld is known to be dependent on the hydrodynamics in the liquid region and the energy transfer in the surrounding heat affected zone. The hydrodynamics in the liquid region, i.e. the weld pool, are dominantly driven by Marangoni convection due to surface tension gradients which are caused by gradients in surface temperature and surface active elements. These dynamics play an important role in the energy transfer to the surrounding metal. The final weld shape, post solidification micro-structures and residual stresses are all determined by these. Therefore, understanding of the fluid and heat flow within the weld pool plus the heat transfer within the heat affected zone is essential in improving weld quality.

Both experimental and numerical studies on weld pool flows and solidification have been carried out over the last decades (e.g. [3, 10, 11, 12, 21]). Experimental measurements on weld pool flows and solidification can be found widely in literature. In general, these researches face three major obstacles: the high temperatures, the small dimensions and the lack of transparency of the weld pool.

In contrast to experiments, numerical studies by the means of Computational Fluid Dynamics (CFD) can easily overcome these obstacles. CFD methods allow for analyzing detailed (time-dependent) solutions for the heat and fluid flow within the weld pool and the energy transfer to the heat affected zone.

Weld pool simulation is not unfamiliar at the department carrying out this project (Transport Phenomena, TU Delft), and over the years several papers have been published on numerical simulation of welding[14, 16, 17, 22]. However, these studies have been limited to spot-welding, whereas a large part of welds in industrial application is performed with a translating heat source.

1.2 Research goal

The main goal in this research is to extend the existing knowledge on spot-welding simulation within the department by adding translation of the heat source. The research

question to be answered to reach that goal is

What are the governing equations for heat transfer, phase change and fluid flow in welding with a heat source moving at constant velocity; and how can these be implemented in an existing OpenFOAM solver?

The duality of this main question is reflected in the report as can be seen in the next section.

1.3 Outline

In Chapter 2, the physical model describing the fluid flow, phase change and heat transfer in a weld pool is presented. This is done both for an inertial frame as for a moving frame of reference. Chapter 3 contains a short introduction to Finite Volume Methods and the numerical implementation of the physical model. In Chapter 4 the results of the multiple validation cases for the modified solver are discussed. The conclusions for this project and the recommendations for further research are presented in Chapter 5.

2 Physical model

2.1 Physical phenomena in a weld pool

The physics of welding is one which includes many coupled phenomena. Figure 2.1 gives an overview of the problem modeled in this research.

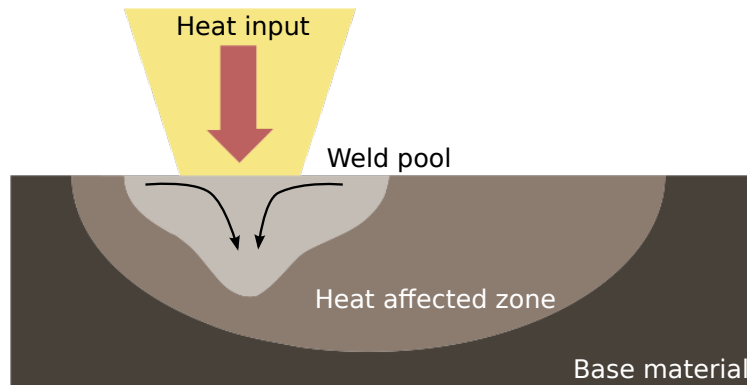


Figure 2.1: Sketch of the weld cross section, showing the weld pool and the heat affected zone. In this sketch the heat source is moving to the left.

An initially solid material is heated by the laser source. When the melting temperature of the material is reached a solid to liquid phase change occurs and the weld pool is formed.

Spatial temperature variations due to the nonuniform heating by the Gaussian laser beam result in significant surface tension gradients. The liquid responds by flowing from regions of low surface tension to regions of high surface tension. This thermo chemical mechanism is called the Marangoni effect and its significance is given by the thermal Marangoni number:

$$Mg = \frac{(d\sigma/dT)L\Delta T}{\mu\alpha} \quad (2.1)$$

The typical Marangoni numbers in laser weld pools are of the order $Mg \sim 10^1 - 10^2$.

Thermal gradients inside the weld pool lead to density gradients which give rise to buoyancy effects. This buoyancy driven flow can be described by the Rayleigh number which itself is the product of the Grashof number with the Prandtl number:

$$Ra = Gr \cdot Pr = \frac{g\beta\Delta TL^3}{\nu^2} \frac{\nu}{\alpha} = \frac{\rho g\beta\Delta TL^3}{\mu\alpha} \quad (2.2)$$

The ratio of the Rayleigh number over the Marangoni number is known as the dynamic Bond number.

$$Bo = \frac{Ra}{Mg} = \frac{\rho g \beta \Delta T L^3 / (\mu \alpha)}{(d\sigma/dT) L \Delta T / (\mu \alpha)} = \frac{\rho g \beta L^2}{(d\sigma/dT)} \quad (2.3)$$

This ratio is typically $10^{-4} - 10^{-3}$ from which it can be concluded that the fluid flow in the weld pool is primary driven by the Marangoni effect. We therefore neglect buoyancy driven flow in this work.

Heat in weld pools is transported by convection and conduction, the ratio of these two mechanisms is given by the Peclet number:

$$Pe = \frac{UL}{\alpha} = \frac{(d\sigma/dT) \Delta T L}{\alpha \mu} \quad (2.4)$$

which is in the order of $10^1 - 10^2$ indicating that convective heat transport is dominant in the weld pool.

The physical model of this research is restricted by the flat surface assumption not allowing any deformations of the weld pool surface. Also mass transfer by evaporation and interfacial reactions are not taken into account.

2.2 Heat transfer

2.2.1 Energy equation

Following the derivations done by Bird, Stewart and Lighthfoot[2], taking into account that the weld pool surface is at atmospheric pressure, we write the energy equation:

$$\frac{\partial}{\partial t}(H) + \nabla \cdot (H\vec{U}) = -\left(\left(\frac{\partial}{\partial t}p + p(\nabla \cdot \vec{U})\right) - (\nabla \cdot \vec{q}) - p(\nabla \cdot \vec{U}) - (\tau : \nabla \vec{U})\right) \quad (2.5)$$

Assuming the fluid to be incompressible and of constant density, the pressure term and the divergence of the velocity are zero. For our application the viscous dissipation term is negligible. Including a source term for the latent heat absorption and release due to the phase change and with $\vec{q} = -\lambda \nabla T$ results in:

$$\frac{\partial}{\partial t}(H) + \nabla \cdot (H\vec{U}) = (\nabla \cdot \lambda \nabla T) + S_{latent} \quad (2.6)$$

and with $H = \rho c_p T$ and constant ρc_p ,

$$\rho c_p \frac{\partial T}{\partial t} + \rho c_p \nabla \cdot (T\vec{U}) = (\nabla \cdot \lambda \nabla T) + S_{latent} \quad (2.7)$$

The heat influx from the laser and the heat outflux at the surface are not incorporated in the energy equation, they are imposed as boundary conditions.

2.2.2 Modeling of the phase change

The absorption of latent heat due to solid to liquid phase change can be implemented in the heat balance in many ways. Because of its rapid convergence and numerical stability the source term method has been chosen for this solver[19].

We start with a simplified energy equation:

$$\frac{\partial H}{\partial t} = \nabla \cdot (\lambda \nabla T) \quad (2.8)$$

For phase change modeling the enthalpy term is split in three parts.

$$H = \rho(1 - g) \int_{T_{ref}}^T c_{p,s} d\xi + \rho g \int_{T_{ref}}^T c_{p,l} d\xi + \rho g L \quad (2.9)$$

Choosing $T_{ref} = 0$ and assuming temperature constant $c_{p,s}$ and $c_{p,l}$ leaves us with:

$$H = \rho(1 - g)c_{p,s}T + \rho g c_{p,l}T + \rho g L \quad (2.10)$$

We plug this relation in to the simplified energy equation.

$$\frac{\partial(\rho(1 - g)c_{p,s}T + \rho g c_{p,l}T + \rho g L)}{\partial t} = \nabla \cdot (\lambda \nabla T) \quad (2.11)$$

For constant ρ and $c_{p,s} = c_{p,l} = c_p$ the equation reduces to

$$\rho c_p \frac{\partial T}{\partial t} + \rho L \frac{\partial g}{\partial t} = \nabla \cdot (\lambda \nabla T) \quad (2.12)$$

the liquid fraction g is a linear function of temperature given by a linear relationship.

$$g(T) = \frac{T - T_s}{T_l - T_s}, T_s \leq T \leq T_l \quad (2.13)$$

It is evident that the absorption of latent heat introduces a non-linearity into the temperature equation. Special treatment of this non-linearity is described in subsection 3.4.1.

2.2.3 Heat influx on the surface

The heat flux into the material is completely determined by the laser. The laser heat flux is assumed to have an ideal radial Gaussian distribution.

$$\Phi_{laser} = a \cdot \exp(-k_q \frac{r^2}{r_q^2}) \quad (2.14)$$

where k_q is the laser beam distribution coefficient and r_q is the laser beam waist radius.

To determine the peak intensity a we look at the power output P of the laser source which is equal to the entire integral over the laser heat flux .

$$P_{laser} = \int_0^\infty \Phi(r) 2\pi r dr = \frac{a\pi r_q^2}{k_q} \quad (2.15)$$

We can see that the peak intensity is a constant depending on the laser power, the beam waist radius and the distribution coefficient. Combining both equations results in the final laser heat flux hence the total heat influx.

$$\Phi_{heat,in} = \frac{k_q P_{laser}}{\pi r_q^2} \exp(-k_q \frac{r^2}{r_q^2}) \quad (2.16)$$

2.2.4 Heat outflux on the surface

The total heat flux out of the material is composed of three different mechanisms: free convection, energy radiation and energy loss due to the evaporation of material.

The convective heat loss can be calculated using

$$\Phi_{convection} = h_c(T_{surface} - T_\infty) \quad (2.17)$$

where h_c is the convection heat transfer coefficient expressing the the heat exchange between the material surface and and the environment.

The energy radiation is given by the Stefan-Boltzmann law.

$$\Phi_{radiation} = \epsilon \sigma (T_{surface}^4 - T_\infty^4) \quad (2.18)$$

In this formula σ is the Stefan-Boltzmann constant and ϵ is the emissivity and the absorption of the material. We assume these to be independent of temperature.

To calculate the heat out flux associated with the evaporation of material we take the relation used by Winkler et al.[20]:

$$\Phi_{evaporation} = W \cdot h_{gf} \quad (2.19)$$

where W denotes the evaporation mass flux and h_{gf} is the heat of evaporation. W is approximated using

$$W = A_1 + \log(p_{atm}) - 0.5 \log(T) \quad (2.20)$$

The constant A_1 varies slightly for different materials. In this thesis the values for iron were used in the calculation. A_1 and h_{gf} become then 2.52 and $6259.5 kJkg^{-1}$. The flux W is given in the unit $kgm^{-2}s^{-1}$. The vapor pressure was obtained in a study by Kim[9].

$$\log(p_{atm}) = 6.1210 - \frac{18836}{T} \quad (2.21)$$

Combining the separate equations for the three different mechanisms results in the total heat outflux.

$$\Phi_{heat,out} = h_c(T_{surface} - T_\infty) + \epsilon \sigma (T_{surface}^4 - T_\infty^4) + W \cdot h_{gf} \quad (2.22)$$

2.3 Fluid flow

2.3.1 Continuity- and momentum equation

Again following the derivations done by Bird, Stewart and Lighthfoot[2], we write the continuity- and the momentum equation.

$$\frac{\partial}{\partial t}\rho + \nabla \cdot (\rho\vec{U}) = 0 \quad (2.23)$$

$$\frac{\partial}{\partial t}\rho\vec{U} + \nabla \cdot (\rho\vec{U}\vec{U}) + \nabla \cdot (\mu\nabla\vec{U}) = \vec{F}_{damp} - \rho\vec{g} - \nabla p \quad (2.24)$$

Where \vec{F}_{damp} is the mushy zone dampening term which is described in the next section. The force \vec{F}_{st} from spatial variations in the surface tension is not incorporated in the momentum equation but imposed as a boundary condition.

2.3.2 Modeling of flow in the mushy zone

Solidification of non-pure materials happens over a range of temperatures, material within this range is mushy - neither solid nor liquid. In this thesis we assume purely columnar growth. In columnar growth solidification happens non-uniformly at the solid boundaries of the domain, leading to columns of solid pointing into the liquid. As solidification only occurs at the solid boundaries, the velocity of the solid part is equal to the velocity of the workpiece. The fluid part is to be modeled analogous to a porous medium. Following the derivations from Darcy's law done by Kidess[8] who includes the dampening force as a source term we end up with.

$$\vec{F}_{damp} \rightarrow \vec{S}_{damp} = -C \frac{(1-g)^2}{g^3 + \epsilon} \vec{U} \quad (2.25)$$

This source term dominates at low liquid fractions over all other terms and forces the fluid velocity to zero near the solid boundary and in the solid.

2.3.3 Modeling of the surface forces

The temperature differences due to the non-uniform heating by the laser source result in a gradient of the surface tension. This gradient gives rise to the Marangoni force which is balanced by the viscous force of the fluid. From this we can compute the liquid velocity gradient at the weld pool surface.

$$\mu \frac{\partial U}{\partial n} = \frac{\partial \sigma}{\partial \tau} = \frac{d\sigma}{dT} \frac{\partial T}{\partial \tau} \quad (2.26)$$

$$\frac{\partial U}{\partial n} = \frac{1}{\mu} \frac{d\sigma}{dT} \frac{\partial T}{\partial \tau} \quad (2.27)$$

Here n and τ denote the normal and tangential vectors of the surface. The surface tension coefficient $\frac{d\sigma}{dT}$ is a function of both temperature and surface active species concentration and is determined following a model by Sahoo [13]:

$$\frac{d\sigma}{dT} = -\frac{d\sigma}{dT}_{pure} - R\Gamma_s \ln(1 + K \cdot a_i) - \frac{K \cdot a_i}{1 + K \cdot a_i} \frac{\Gamma_s \Delta H^0}{T} \quad (2.28)$$

Where $\frac{d\sigma}{dT}_{pure}$ is the surface tension coefficient of the pure material, R is the ideal gas constant, Γ_s is the surface saturated excess concentration of surfactant, K the equilibrium constant for the absorption reaction, a_i the activity of the surfactant species and ΔH^0 the heat adsorption.

This model given by Sahoo can give rise to three possible surface tension coefficients which all three lead to different flow configurations as can be seen in figure 2.2. The fluid flow is always in the direction from low to high surface tension.

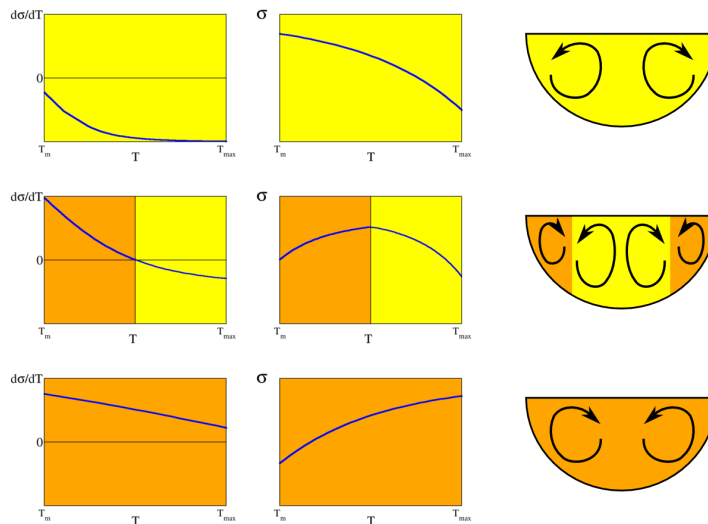


Figure 2.2: Illustration of the relation between the temperature gradient of surface tension between the melting temperature T_m and the the maximum weld pool temperature T_{max} , and the Marangoni driven flow directions.[15]

2.4 Moving frame of reference

In order to minimize the necessary grid size for simulation and achieve a sufficient weld pool resolution without the need of excess computer power the solver is formulated in a moving frame of reference. The common choice is to attach the coordinate system to the moving laser source [3, 10]. To keep the convective velocity as the primary unknown in the governing equation we define a net velocity which is the sum of the convective velocity and the constant welding velocity of the laser:

$$\vec{V} = \vec{U} + \vec{U}_t \quad (2.29)$$

All the previous governing equations are transformed to the moving frame reference using this relation. The derivations are given in the appendix, the final forms of the new equations are given below.

$$\frac{\partial}{\partial t} \rho + \nabla \cdot (\rho \vec{U}) = 0 \quad (2.30)$$

$$\rho c_p \frac{\partial T}{\partial t} + \rho L \frac{\partial g}{\partial t} + \nabla \cdot (\rho c_p T \vec{U}) + \nabla \cdot (\rho c_p T \vec{U}_t) + \nabla \cdot (\rho g L \vec{U}) = (\nabla \cdot \lambda \nabla T) \quad (2.31)$$

$$\frac{\partial}{\partial t} \rho \vec{U} + \nabla \cdot (\rho \vec{U} \vec{U}) + \nabla \cdot (\rho \vec{U}_t \vec{U}) + \mu \nabla^2 \vec{U} = -C \frac{(1-g)^2}{g^3 + \epsilon} \vec{U} - \rho \vec{g} - \nabla p \quad (2.32)$$

3 Numerical implementation

3.1 Finite Volume Method

The governing equations derived in chapter 2 are solved numerically by means of the Finite Volume Method (FVM) implemented in the CFD framework OpenFOAM. The principle behind the FVM is to integrate the equations over a finite number of control volumes and solve the equations in the integral form.

The continuity, momentum and heat equation are conservation equations and can all be rewritten in the generic conservation equation

$$\frac{\partial(\rho C_\phi \phi)}{\partial t} + \nabla \cdot (\rho C_\phi \phi \vec{U}) = (\nabla \cdot \Gamma_\phi \nabla \phi) + S_\phi \quad (3.1)$$

where ϕ is the generic variable, Γ_ϕ the diffusion coefficient associated with the generic variable, and S_ϕ the source term.

The generic conservation equation can, with use of the divergence theorem, be rewritten in the integral form as follows:

$$\underbrace{\frac{\partial}{\partial t} \int_V \rho C_\phi \phi dV}_{Unsteady} + \underbrace{\int_S \rho C_\phi \phi \vec{U} \cdot d\vec{S}}_{Convection} = \underbrace{\int_S \Gamma_\phi \nabla \phi \cdot d\vec{S}}_{Diffusion} + \underbrace{\int_V S_\phi dV}_{Source} \quad (3.2)$$

3.1.1 Spatial discretization

The unsteady and source terms in the integral form of the generic equation are evaluated at the control volume center, the convection and diffusion terms are evaluated at the control volume surface. In the CFD framework used in this thesis all dependent variables are stored at the cell centers. Therefore some interpolation is needed to express the cell surface values in terms of the cell center values. Different interpolation schemes are available in the OpenFOAM framework:

Central Differencing In the the Central Differencing (CD) scheme linear interpolation between the two adjacent cell center values determines the cell surface value. The CD scheme is second order-accurate but unbounded[1].

$$\phi_e = f_e \phi_P + (1 - f_e) \phi_E \quad (3.3)$$

with $f_e = \overline{fE}/\overline{PE}$ where \overline{fE} is the distance between face f and cell center E and \overline{PE} is the distance between cell centers P and E .

Upwind Differencing In the the Upwind Differencing (UD) scheme the cell surface value is determined by the flow direction. The UD scheme is bounded at the expense of accuracy[1].

$$\phi_e = \begin{cases} \phi_E, & v_e < 0 \\ \phi_P, & v_e \geq 0 \end{cases} \quad (3.4)$$

Minmod The Minmod scheme is combines the Central Differencing scheme and Upwind Difference scheme. The Minmod scheme is an attempt to preserve boundedness with reasonable accuracy[1].

$$\phi_e = (1 - \gamma)(\phi_e)_{UD} + \gamma(\phi_e)_{CD} \quad (3.5)$$

with

$$\gamma = \max \left[0, \min \left[1, \frac{\phi_P - \phi_E}{\phi_E - \phi_W} \right] \right] \quad (3.6)$$

In this thesis the interpolation is performed using the Central Differencing scheme and the Minmod scheme. The CD scheme is used for gradients and the Minmod scheme is used for the divergence.

3.1.2 Time integration

The unsteady term in the integral form of the generic conservation equation can be discretized in an implicit or an explicit manner. In this thesis we implemented the implicit 2nd-order backward differencing scheme:[7]

$$\frac{\partial}{\partial t} \int_V \rho \phi dV = \frac{3(\rho_P \phi_P V)^n - 4(\rho_P \phi_P V)^0 + (\rho_P \phi_P V)^{00}}{2\Delta t} \quad (3.7)$$

where n , 0, 00 represent the new, the last and the before last time step.

3.2 Mesh

For the simulations in this thesis 3D rectilinear meshes are used. Figure 3.1 shows a coarse version for clarity of the top and side view of a typically used mesh.

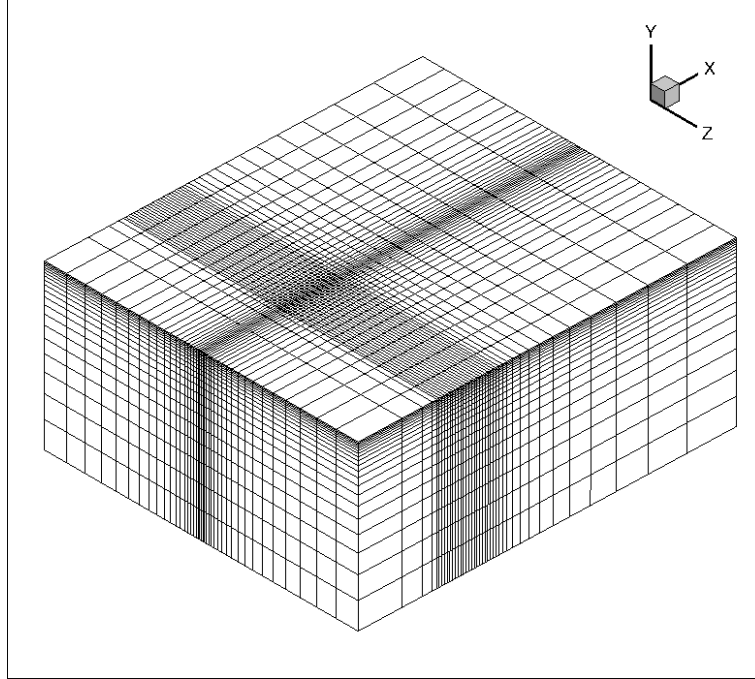


Figure 3.1: Coarse version of a typical 3D symmetric mesh ($n_x \times n_y \times n_z = 40 \times 20 \times 20$) used for validation.

The heat flow through the material determines the minimum range of the mesh. To prevent the influence of boundary effects on the solution we choose the minimum distance from the laser spot center to the boundary of the mesh to be twice the penetration depth:

$$\delta = \sqrt{\pi\alpha t} \quad (3.8)$$

In our simulations, where the steady state is reached after $t = 1.5s$, the distance from the laser spot center to the boundary should be at least $2\delta \sim 10mm$.

As can be seen in figure 3.1, cell sizes are not uniform throughout the computational domain. The optimal cell size is a trade off between several properties and varies by location

- Computational cell size is inversely proportional to the resolution of the simulation. Especially in the weld pool area, where the gradients are relatively large, the resolution is of great importance.
- Smaller cells evidently result in a higher total amount of cells which again result in a higher demand of computational power.
- The Courant-Friedrichs-Lewy (CFL) condition for stability states $Co = \frac{U\Delta t}{\Delta x} \leq Co_{max} \leq 1$. Increasing the number of computational cells results in a smaller characteristic length and a smaller time step leading to a higher computer load.

The characteristic refinement of the mesh towards the center of the top surface is a result of attaching the mesh to the moving heat source. With this decision the weld pool is always located on the same spot and therefore limiting the total area where high resolution is needed.

3.3 Boundary conditions

We incorporate two different thermal boundary conditions which both depend on the first derivative of temperature. In sections 2.2.3 and 2.2.4 we determined the heat influx and outflux through the material surface. Combining these two results in the total heat flux through the top boundary.

$$\Phi_{total} = \Phi_{in} - \Phi_{out} = \frac{k_q P}{\pi r_q^2} \exp(-k_q \frac{r^2}{r_q^2}) - h_c(T_{surface} - T_\infty) - \epsilon \sigma (T_{surface}^4 - T_\infty^4) - W \cdot h_{gf} = \lambda \frac{dT}{dn} \Big|_{surface} \quad (3.9)$$

which is rewritten in the Neumann boundary condition.

$$\frac{dT}{dn} = \frac{1}{\lambda} \Phi_{total} \quad (3.10)$$

We assume that the side and bottom boundaries are too far away from the weld pool to be affected by the weld pool heat, therefore we impose adiabatic boundary condition:

$$\nabla T = 0 \quad (3.11)$$

Boundary conditions for the convective velocity U are defined in a similar way. In section 2.3.3 we defined the derivative of the convective velocity at the weld pool surface:

$$\frac{\partial U}{\partial n} = \frac{1}{\mu} \frac{d\sigma}{dT} \frac{\partial T}{\partial \tau} \quad (3.12)$$

The side and bottom boundary are not affected by the weld pool heat and will always remain solid. The velocity on the side and bottom boundary will not change over time or location. We therefore impose a zero gradient condition.

$$\frac{\partial U}{\partial \tau} = 0 \quad (3.13)$$

3.4 Solver details

The previous three sections described how to transform the problem from the physical domain to the computational the domain. This section deals with specific characteristics of the solver used in this thesis.

3.4.1 Splitting the energy source term

The source term S_{latent} in the energy equation accounts for the evolution of the latent heat during solid-to-liquid phase change. To reduce the computational cost of solving this non-linear source term we implement the source term linearization technique [18]. In this technique non-linearities are accounted for through iterations of the following linearization:

$$S_{latent} = S_P T + S_C \quad (3.14)$$

The coefficients S_P and S_C are defined as:

$$S_p = -\frac{\rho L}{\Delta t} \frac{\partial F}{\partial T} \quad (3.15)$$

$$S_c = -S_p F^{-1} + \frac{\rho L}{\Delta t} (g^{old} - g) \quad (3.16)$$

with liquid fraction profile F and the inverse function F^{-1} are defined as:

$$\frac{\partial F(T)}{\partial T} = \frac{1}{(T_l - T_s)} \quad (3.17)$$

and

$$F^{-1} = F^{-1}(g) = g^{old}(T_l - T_s) + T_s \quad (3.18)$$

Together these equations form the iteration scheme for the temperature T and the liquid fraction g .

3.4.2 Computation sequence

The computation sequence is summarized in the flow chart in figure 3.2.

The computation is always preceded by the pre-processing phase. In this phase the computational mesh is generated, quality control is of great importance since the reliability of the result tremendously relies on the sufficient quality of the mesh.

The main computation phase starts off with the field initialization, during this step the initial and boundary conditions are applied to the mesh.

Solving the momentum equation requires the pressure field to be known beforehand, however the pressure field is derived again from the continuity and momentum equation. This introduces the pressure velocity coupling which we solve with the PISO algorithm (pressure implicit with splitting of operator) proposed by Issa in 1985 [6].

As mentioned already in section 3.4.1, the energy equation and the liquid fraction are also dependent on one another and are solved by the iteration scheme proposed in the same section.

After finishing the main computation, the time-dependent results are processed by means of field visualization and plots of variable distribution or time dependency.

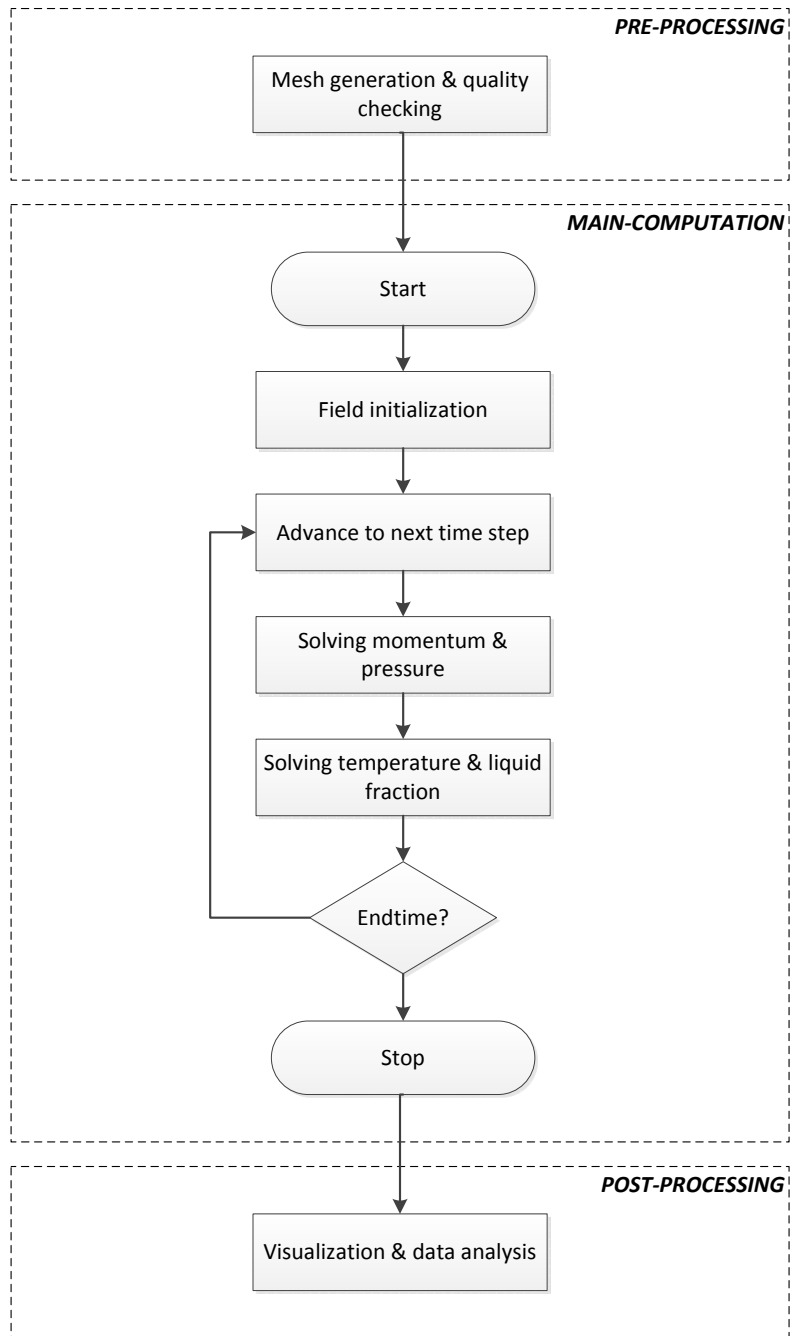


Figure 3.2: Flow chart describing the stages and steps in the simulation process

4 Validation

This chapter reports the validation cases for the implementation of a moving reference frame. For the convenience of the reader, each case is described in a similar way. First the physical and numerical frame work is outlined and the expected results are expressed. After that the numerical results are compared with the theoretical expectation.

The validation consists of three types of test cases; First we compare simulations with analytical solutions of thermal conduction problems. After that we test the change in frame of reference by running equivalent cases with the original and the modified solver. In the end we test nine relevant case set ups and compare the behavior of the fluid flow with our expectations.

4.1 Validation of thermal conduction

4.1.1 Stationary heat source

For the first case we consider spherical thermal conduction due to the continuous release of heat by a stationary point source.

Physical framework

The analytical solution to this problem is given by Hoogendoorn [5]:

$$T(r, t) = \frac{P_{source}}{4\pi\lambda r} \operatorname{erfc}\left(\frac{r}{\sqrt{4at}}\right) \quad (4.1)$$

We rewrite this formula to:

$$T(r, t) = \frac{P_{laser}}{2\pi\lambda r} \operatorname{erfc}\left(\frac{r}{\sqrt{4at}}\right) + T_{\infty} \quad (4.2)$$

Where T_{∞} is the initial temperature of the material and $P_{source} = 2 \cdot P_{laser}$ since we simulate only half of the material. With these adjustments we can compare the analytical solution with the following simulations:

1. Continuous heating of the material by a stationary point laser source without melting.
2. Continuous heating of the material by a stationary point laser source with melting but without latent heat absorption or fluid flow.

We expect the numerical results and analytical solution to yield the same result and thereby validate the solvers ability to cope correctly with thermal conduction.

Numerical framework

In both simulations we use the same mesh which is similar to the example in figure 4.1 but also symmetric in the x-direction. The computational domain of $(40 \times 40 \times 20)$ mm is divided in $(110 \times 60 \times 22)$ cells which result in a minimum cell volume of 0.00121 mm^3 .

The thermal and velocity boundary conditions are specified as in section 3.3 except for the heat flux through the top surface, only the laser heat influx is taken into account. The convection, radiation and evaporation are set to zero since they not appear in the analytical solution. The point source characteristic of this heat influx is achieved by setting $r_q^2 = 0.25 \text{ mm}^2$.

Result and discussion

Since only thermal conduction is considered in this case the temperature profiles are used to compare both simulations with the analytical solution, these profiles are shown in figure 4.1.

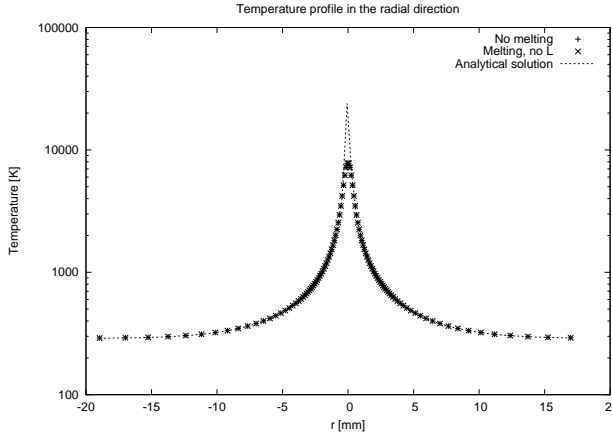


Figure 4.1: Plot of the temperature profile in the radial direction for the analytical solution and both simulations at $t = 5.0s$.

As expected the results for both numerical cases almost perfectly agree with the analytical solution. They only differ near the origin where the analytical solution diverges due to the point source characteristic. Ignoring this unphysical behavior of the analytical solution we can safely state that the solver correctly copes with thermal conduction for a stationary heat source.

Since we are simulating a radially symmetric solution on a square mesh it is very important for the computational domain to be chosen large enough such that the boundary conditions do not interfere with solution.

4.1.2 Moving heat source

In the second case we again consider spherical thermal conduction due to the continuous release of heat by a point source. But now the material is translating with constant velocity U_t in the positive x-direction.

Physical framework

The analytical steady state solution to this problem is also given in by Hoogendoorn [5]:

$$T(r) = \frac{P_{source}}{4\pi\lambda\sqrt{x^2 + y^2 + z^2}} \exp\left(-\frac{U_t(\sqrt{x^2 + y^2 + z^2} - x)}{2a}\right) \quad (4.3)$$

Which is rewritten as in the previous section

$$T(r) = \frac{P_{laser}}{2\pi\lambda\sqrt{x^2 + y^2 + z^2}} \exp\left(-\frac{U_t(\sqrt{x^2 + y^2 + z^2} - x)}{2a}\right) + T_\infty \quad (4.4)$$

The two analogous cases to this analytical solution are:

1. Continuous heating of the material by a moving point laser source without melting.
2. Continuous heating of the material by a moving point laser source with melting but without latent heat absorption or fluid flow.

Like in the previous case we expect the numerical results to be in agreement with the theoretical solution. However in this case we compare the simulation results with a long time steady state solution.

Numerical framework

In both cases the computational domain is (50x40x20) mm which is split in (60x44x22) cells resulting in a minimum cell volume of 0.00192 mm³. The thermal and velocity boundary conditions are specified as in the previous validations case.

Result and discussion

For comparing the results we look at the temperature profiles, longitudinal and transverse to the translation direction of the material, which are shown in figure 4.2.

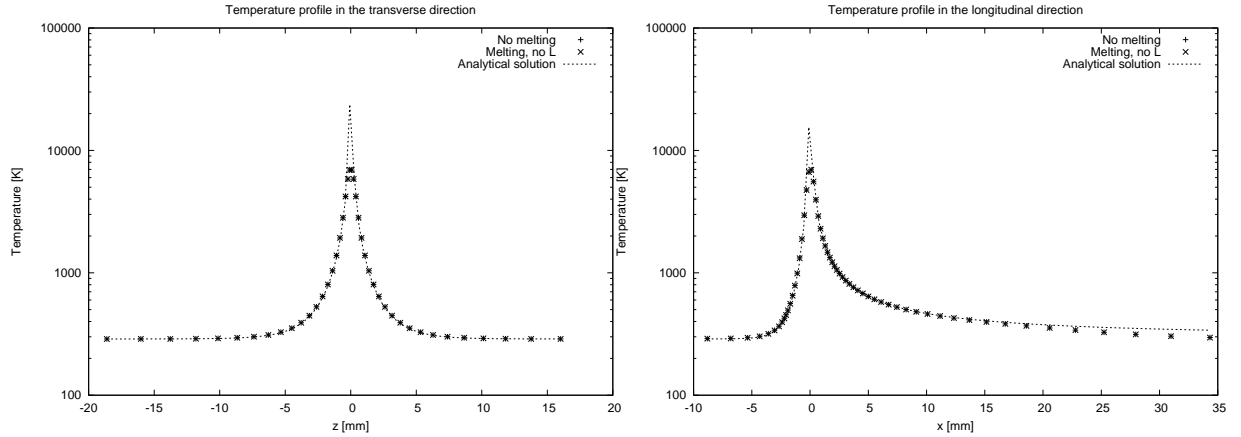


Figure 4.2: Temperature profile for the analytical solution and for both simulations at $t = 5.0s$. On the left is the transverse profile and the right is in the longitudinal direction

In the left plot of figure 4.2 we see that the temperature profile in the transverse direction is full developed for both cases. In the right plot we see that the temperature profile in the longitudinal directions matches the steady state solution near the heat source but diverges in the long tail. This can be explained by the simulation time of 5.0 seconds, which is not enough for the temperature profile to fully converge to the steady state solution

Again ignoring the unphysical behavior of the analytical solution near the origin we can also state that the solver correctly copes with thermal conduction for a moving heat source.

4.2 Validation of convective heat flow

In the previous section we successfully validated the solver for thermal conduction with a stationary and a moving heat source. From experience we know that heat transfer within the weld pool is mainly driven by convective flow. The solvers ability to cope with this convective flow is tested in this chapter by comparing simulation results of the original benchmarked solver and modified solver.

4.2.1 Stationary heat source

In this case we compare the results of both solvers for welding in the situation where the laser is stationary.

Physical framework

The difference between both solvers is the frame of reference they operate in. The original solver is attached to the material, the modified solver to the heat source. For a stationary heat source, i.e. setting the translation velocity \vec{U}_t to zero, both frames of reference are identical. Therefore the results of simulations run on the same mesh with the same thermal and velocity boundary conditions should be identical too.

Numerical framework

The mesh we use is similar to the example in figure 4.1. The computational domain of (20x20x10) mm is divided in (108x80x40) cells which result in a minimum cell volume of $6.38 \times 10^{-5} \text{ mm}^3$. The thermal and velocity boundary conditions are specified as described in section 3.3.

Result and discussion

The three most interesting properties generated by our solver are; the temperature distribution in the material, the fluid flow in the weld pool and the shape of the weld pool. Since the latter is fully dependent on the first two we take the weld pool shape as the benchmark for comparing simulation results.

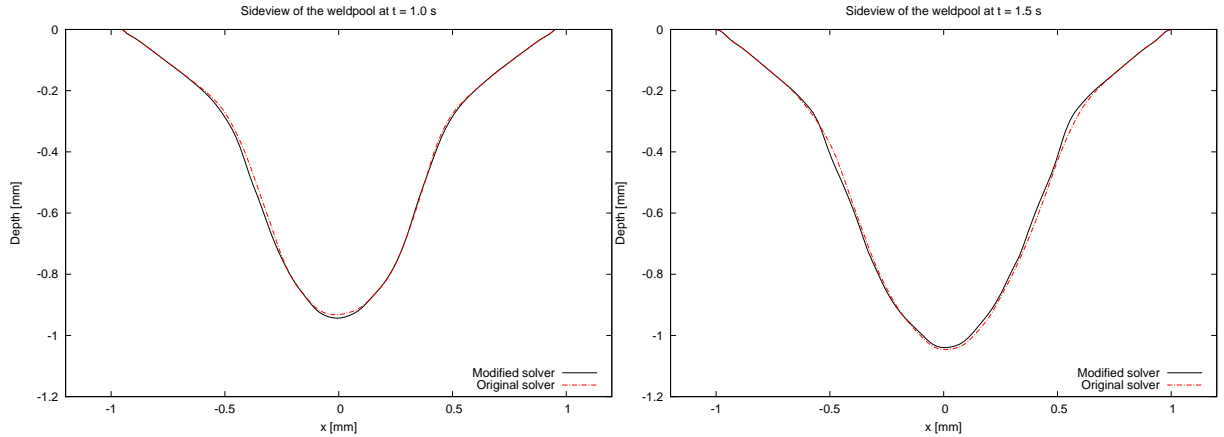


Figure 4.3: 2D plot of the weld pool shapes for $t = 1.0s$ and $t = 1.5s$.

Figure 4.3 presents the results generated by the original and modified solver. For both $t = 1.0s$ and $t = 1.5s$ the weld pool shapes are virtually identical, the small differences between both shapes don't increase in time. The maximum cell length in the weld pool area is almost 0.1 mm, which is in the order of the differences in both simulations. Therefore we conclude that the modified solver correctly copes with Marangoni driven fluid flow in welding with a stationary heat source.

4.2.2 Moving heat source

The motivation to modify the original solver is to reduce the amount of computational cells needed and thereby reduce the required computer power. Therefore in section 2.4 we rewrote the governing equations to the reference frame of the moving heat source. The goal of this case is to justify this choice.

Physical framework

For the validation of the convective heat flow with a moving heat source we compare two cases:

1. In the frame of reference of the material we let the heat source translate with U_t in the negative x-direction, i.e. using the original solver.
2. In the frame of reference of the heat source we let the material translate with U_t in the positive x-direction, i.e. using the modified solver.

Physically these two situations are equivalent and therefore they should yield the same weld pool shape. The welding speed in both cases is set to 1 mms^{-1} which is common in ordinary welding.

Numerical framework

For the first case the computational domain of $(17.5 \times 20 \times 10)$ mm consists of $(130 \times 80 \times 40)$ cells, for the second case the domain of $(20 \times 20 \times 10)$ mm is divided in $(116 \times 80 \times 40)$ cells. The resulting minimum cell volumes are $6.32 \times 10^{-5} \text{ mm}^3$ and $5.76 \times 10^{-5} \text{ mm}^3$.

The thermal and velocity boundary conditions for both cases are specified as in section 3.3 except for the heat influx through the top surface for the case in the reference frame of the material. This heat influx is the heat source and should be moving in the negative x-direction. To achieve this we apply the coordinate transform $r \rightarrow r + \vec{U}_t t$ resulting in the new, time dependent, heat influx.

$$\Phi_{heat,in}(t) = \frac{k_q P}{\pi r_q^2} \exp\left(-k_q \frac{(r + \vec{U}_t t)^2}{r_q^2}\right) \quad (4.5)$$

Result and discussion

As in the previous validation regarding the ability to cope with fluid flow we again take the weld pool shape as the benchmark for comparing both simulations

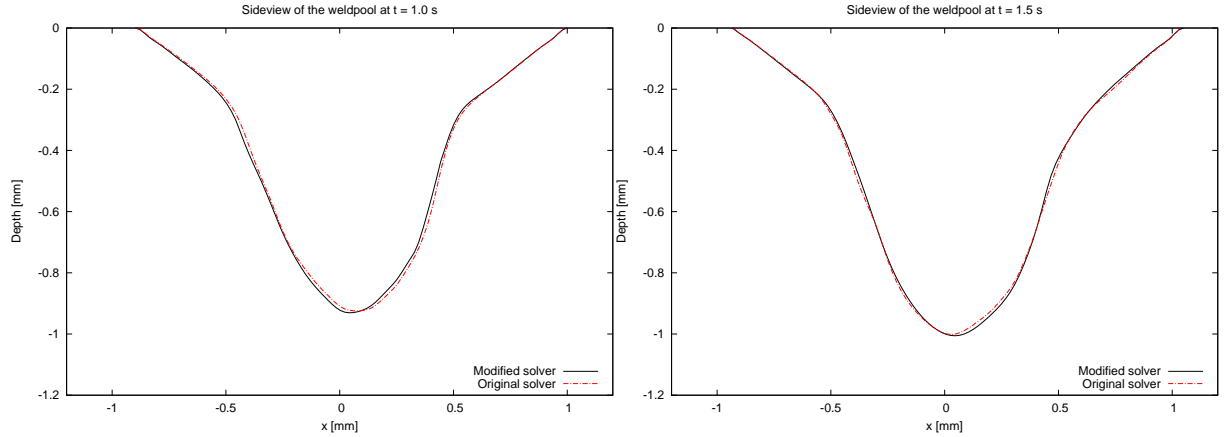


Figure 4.4: Plot of the weld pool shapes for $t = 1.0s$ and $t = 1.5s$.

In figure 4.4 we see a comparison of the weld pool shapes generated. Both at $t = 1.0s$ and at $t = 1.5s$ the results are close to identical and the small error isn't increasing in time. Therefore we conclude that the modified solver correctly copes with Marangoni driven fluid flow in welding with a moving heat source too.

Since we now have two similar case set ups simulated on a different mesh due to the different frame of reference in which the solver operates, we are able to verify if the modified solver has a computational advantage over the original solver.

- Both simulations were run on the same computer cluster using the same amount of CPU's.
- The original OpenFOAM solver required 416000 computational cells leading to an execution-time of 167463 seconds.
- The modified OpenFOAM solver required 371200 computational cells leading to an execution-time of 146531 seconds.

The modified solver required 10.8% less computational cells for the same simulation as the original solver and took 12.5% less time to arrive at this result. For higher welding velocities and longer simulations these numbers will only increase in favor of the modified solver.

4.3 Welding simulations with a moving heat source and fluid flow

In this section we discuss simulation results generated by the modified solver. We have opted for three different heat source velocities and three different surface tension coefficients resulting in a total of nine cases to be discussed.

Physical framework

First we discuss the influence of the heat source velocity on the simulation result. In all cases we use the same laser source, i.e. the same heat influx. Increasing the heat source velocity leads to the laser power being distributed over a larger area which results in a lower average energy input per volume.

We therefore expect the weld pool size and maximum temperature to decrease for higher heat source velocities.

The influence of the three possible surface tension coefficients on the fluid flow pattern in the weld pool is neatly depicted in figure 2.2 in subsection 2.3.3. Since heat transfer in the weld pool is dominated by convection we expect the surface tension coefficient to have a major effect on the weld pool size.

A negative surface tension coefficient leads to surface fluid flow transporting the inserted heat away from the laser source, we therefore expect a wide shallow weld pool. With a positive surface tension coefficient the surface fluid flows are directed toward the laser source and forced down in the weld pool, here we expect a narrower and deeper weld pool.

We expect the temperature near the weld pool to follow the shape of the weld pool, further away we expect it to converge to the analytical solutions given in section 4.1.

Numerical framework

The computational domain and the number of cells used in each simulation can be found above the plots of the corresponding results. Side views of the meshes used in the simulations are shown in figure 4.5.

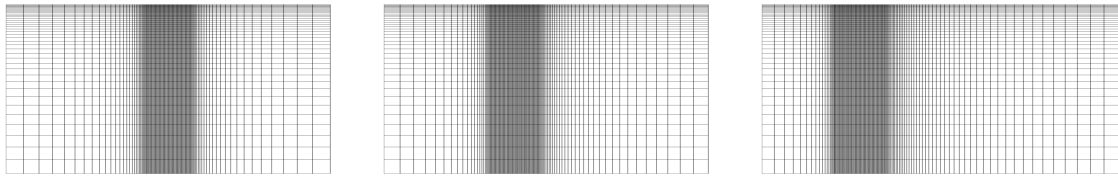


Figure 4.5: Side views of the mesh used in the simulation with: $U_t = 0 \text{ mms}^{-1}$, $U_t = 1 \text{ mms}^{-1}$ and $U_t = 5 \text{ mms}^{-1}$.

The thermal and velocity boundary conditions are specified as described in section 3.3.

Result and discussion

The results of the nine simulations are presented in the figures 4.6 to 4.14, a combined overview of these results can be found in figures 6.1, 6.2 and 6.3 in the appendix.

Looking at the results from all nine simulations we can directly see that the size of the weld pool is highly influenced by the speed of the moving heat source. As expected, the depth and width of the weld pool decrease for higher welding speeds. Our expectations regarding the positive and negative surface tension coefficients are confirmed. Also the

deformation of the temperature profile due to the welding velocity and the weld pool shape is clearly visible.

Interesting to see is the symmetry breaking in the welding simulations with a stationary heat source, especially for the positive surface tension coefficient. This symmetry breaking was also detected by Saldi[15]. The symmetry breaking may be of physical or numerical origin. The high fidelity simulations necessary to rule out numerical instabilities are out of the scope of this thesis.

Case	$U_{t,x}$	$d\sigma/dT$	Computational Domain	# Cells
1.1	0 mms^{-1}	+	20 x 20 x 10 mm	104 x 80 x 40
1.2	1 mms^{-1}	+	20 x 20 x 10 mm	116 x 80 x 40
1.3	5 mms^{-1}	+	22 x 20 x 10 mm	128 x 80 x 40

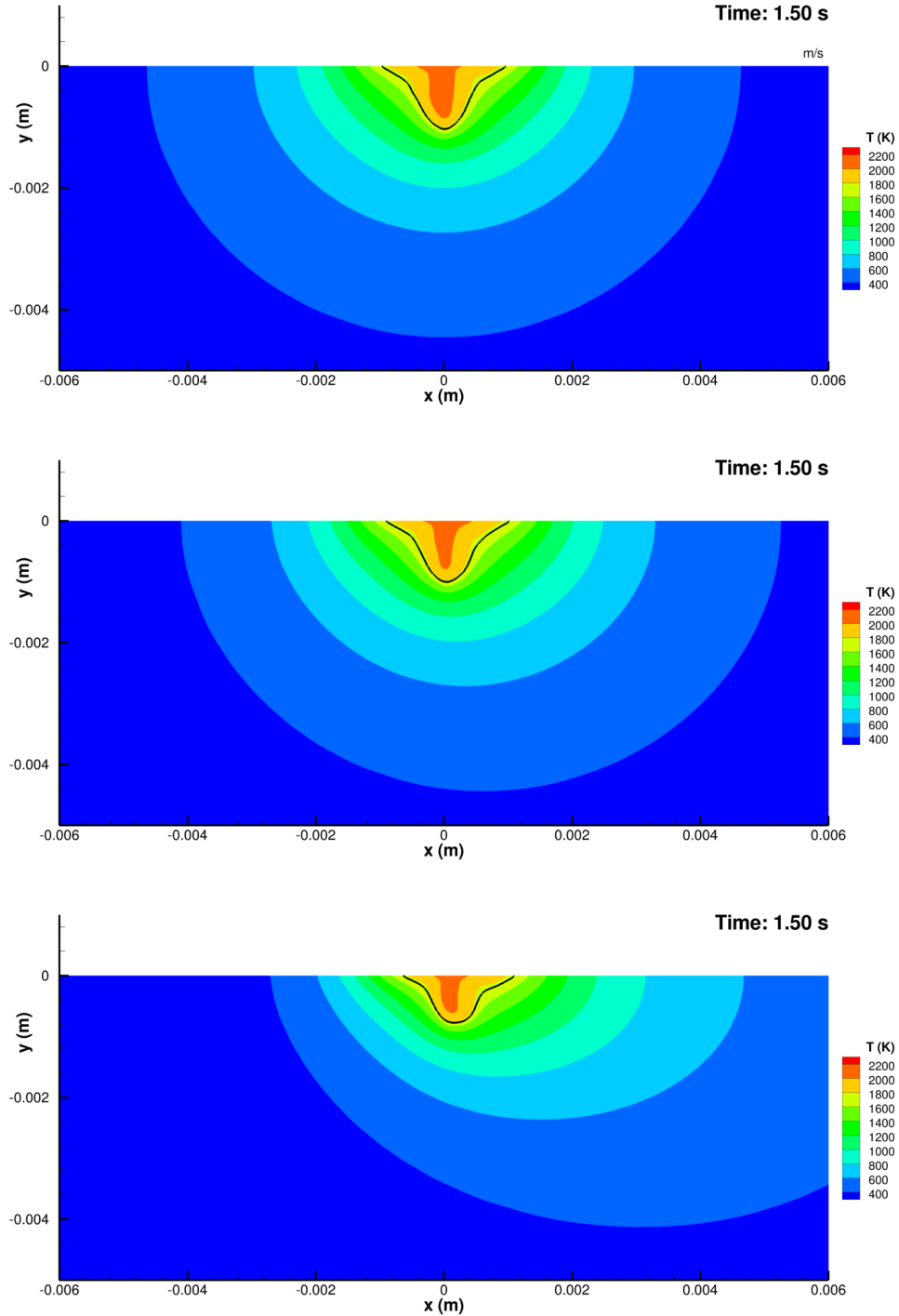


Figure 4.6: The side views of the temperature profile of three cases with a positive $d\sigma/dT$

Case	$U_{t,x}$	$d\sigma/dT$	Computational Domain	# Cells
1.1	0 mms^{-1}	+	20 x 20 x 10 mm	104 x 80 x 40
1.2	1 mms^{-1}	+	20 x 20 x 10 mm	116 x 80 x 40
1.3	5 mms^{-1}	+	22 x 20 x 10 mm	128 x 80 x 40

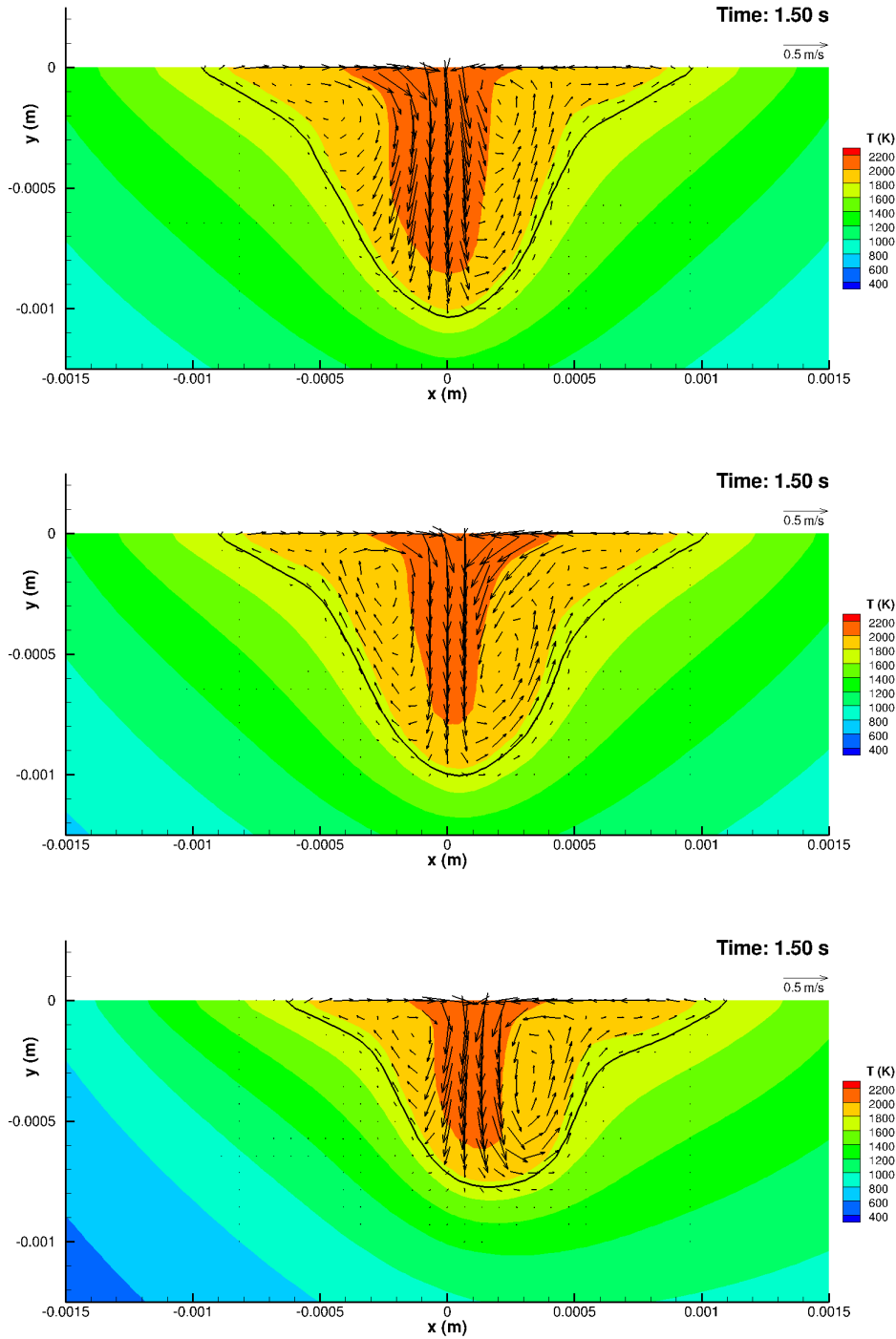


Figure 4.7: The side views of the weld pools of three cases with a positive $d\sigma/dT$

Case	$U_{t,x}$	$d\sigma/dT$	Computational Domain	# Cells
1.1	0 mms^{-1}	+	20 x 20 x 10 mm	104 x 80 x 40
1.2	1 mms^{-1}	+	20 x 20 x 10 mm	116 x 80 x 40
1.3	5 mms^{-1}	+	22 x 20 x 10 mm	128 x 80 x 40

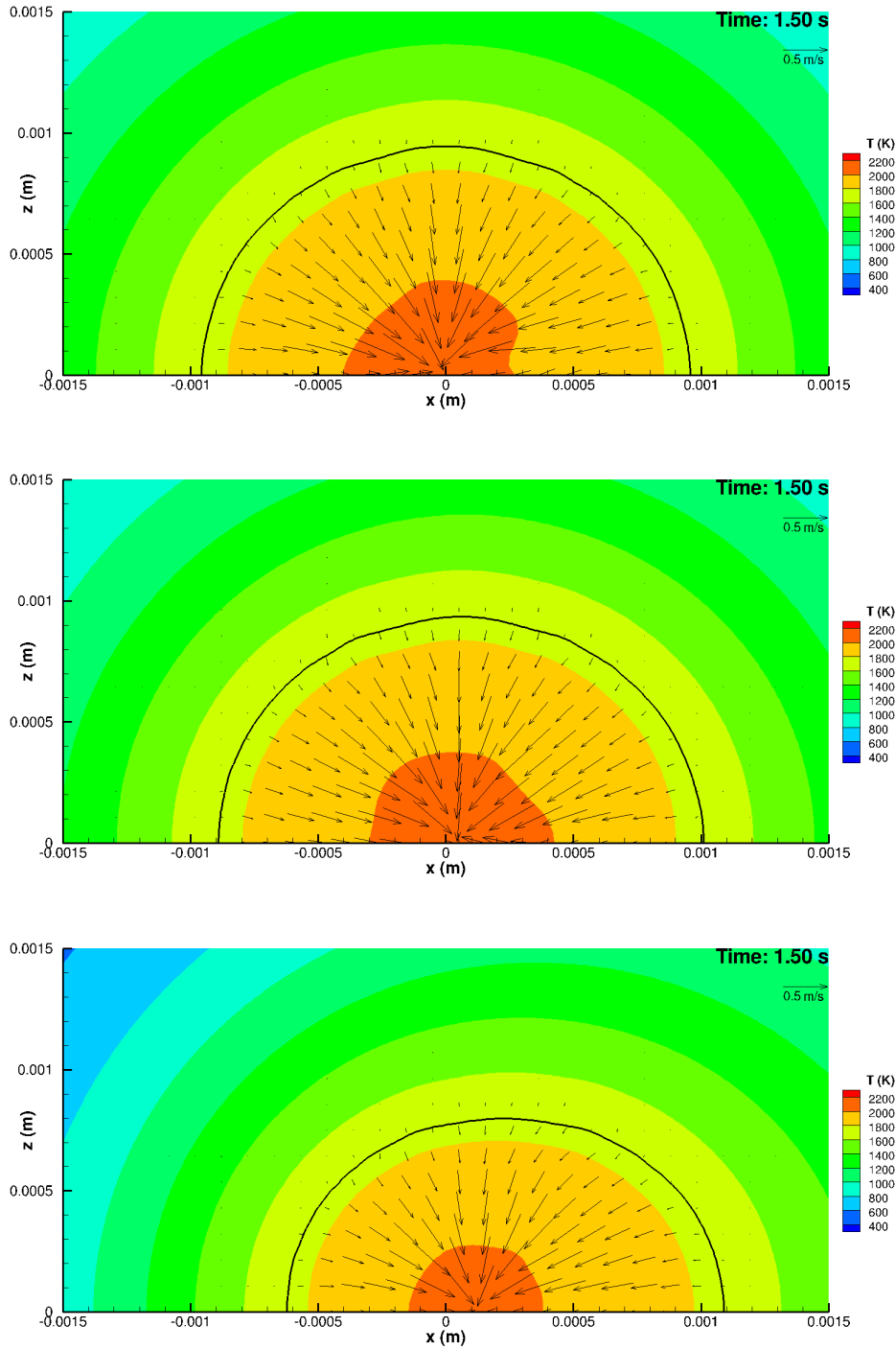


Figure 4.8: The top views of the weld pools of three cases with a positive $d\sigma/dT$

Case	$U_{t,x}$	$d\sigma/dT$	Computational Domain	# Cells
2.1	0 mms^{-1}	-	20 x 20 x 10 mm	104 x 80 x 60
2.2	1 mms^{-1}	-	20 x 20 x 10 mm	116 x 80 x 60
2.3	5 mms^{-1}	-	22 x 20 x 10 mm	128 x 80 x 60

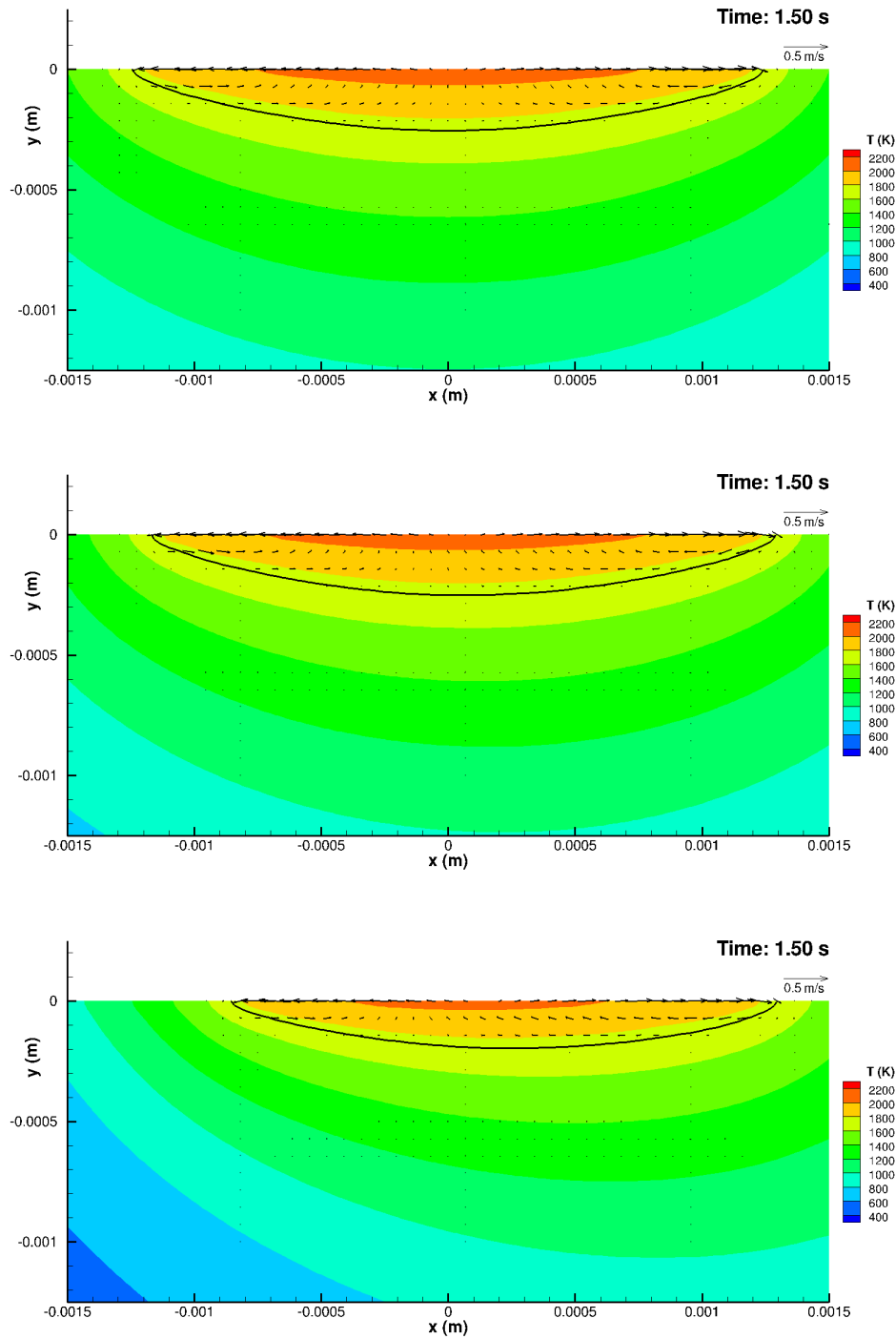


Figure 4.10: The side views of the weld pools of three cases with a negative $d\sigma/dT$

Case	$U_{t,x}$	$d\sigma/dT$	Computational Domain	# Cells
2.1	0 mms^{-1}	-	20 x 20 x 10 mm	104 x 80 x 60
2.2	1 mms^{-1}	-	20 x 20 x 10 mm	116 x 80 x 60
2.3	5 mms^{-1}	-	22 x 20 x 10 mm	128 x 80 x 60

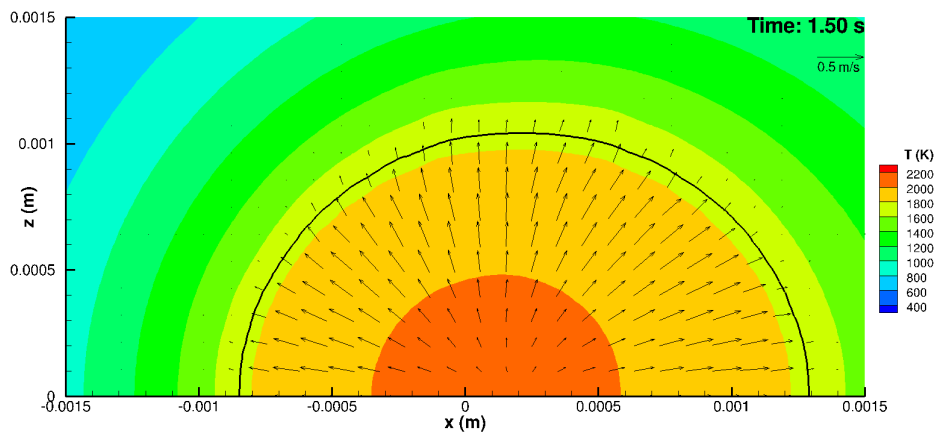
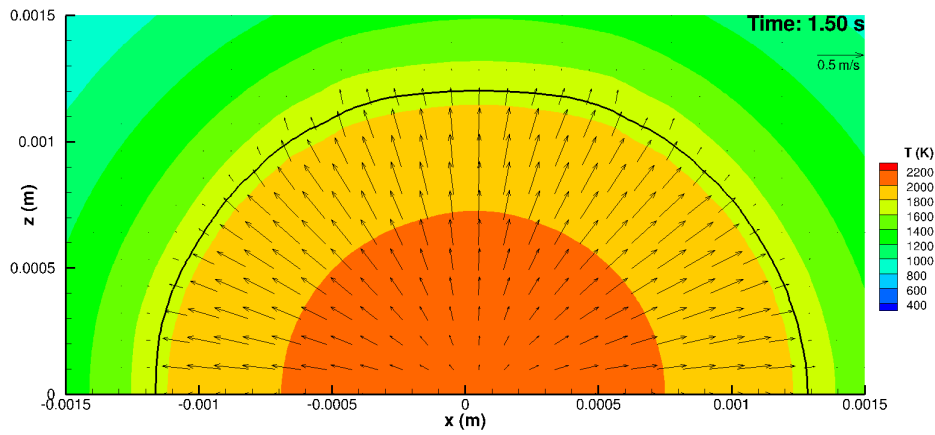
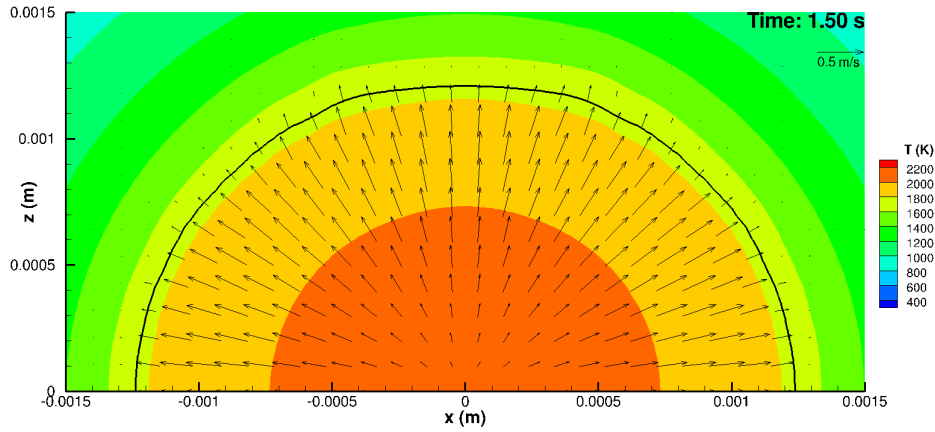


Figure 4.11: The top views of the weld pools of three cases with a negative $d\sigma/dT$

Case	$U_{t,x}$	$d\sigma/dT$	Computational Domain	# Cells
3.1	0 mms^{-1}	+/-	20 x 20 x 10 mm	104 x 80 x 40
3.2	1 mms^{-1}	+/-	20 x 20 x 10 mm	116 x 80 x 40
3.3	5 mms^{-1}	+/-	22 x 20 x 10 mm	128 x 80 x 40

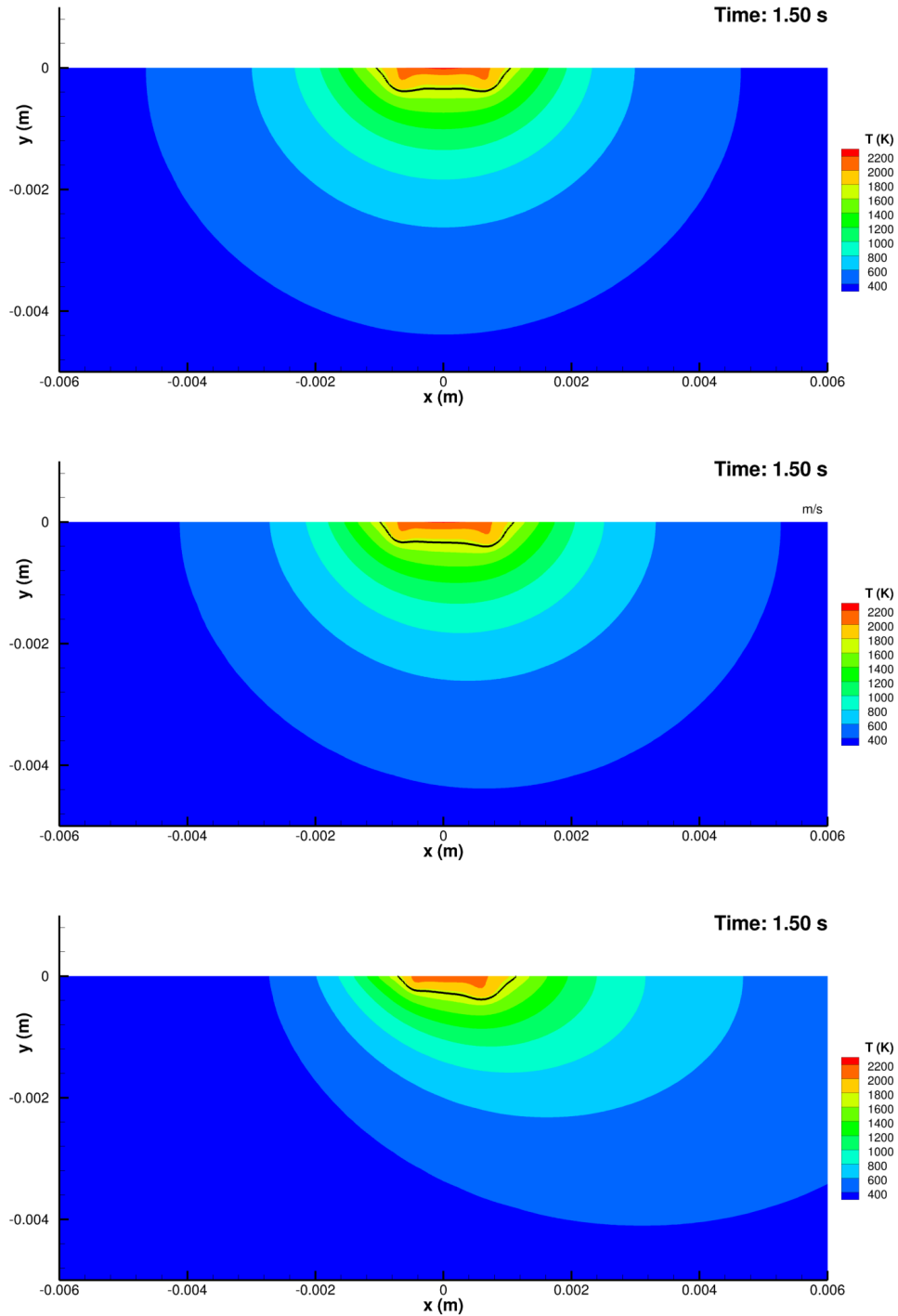


Figure 4.12: The side views of the temperature profile of three cases with a sign changing $d\sigma/dT$

Case	$U_{t,x}$	$d\sigma/dT$	Computational Domain	# Cells
3.1	0 mms^{-1}	+/-	20 x 20 x 10 mm	104 x 80 x 40
3.2	1 mms^{-1}	+/-	20 x 20 x 10 mm	116 x 80 x 40
3.3	5 mms^{-1}	+/-	22 x 20 x 10 mm	128 x 80 x 40

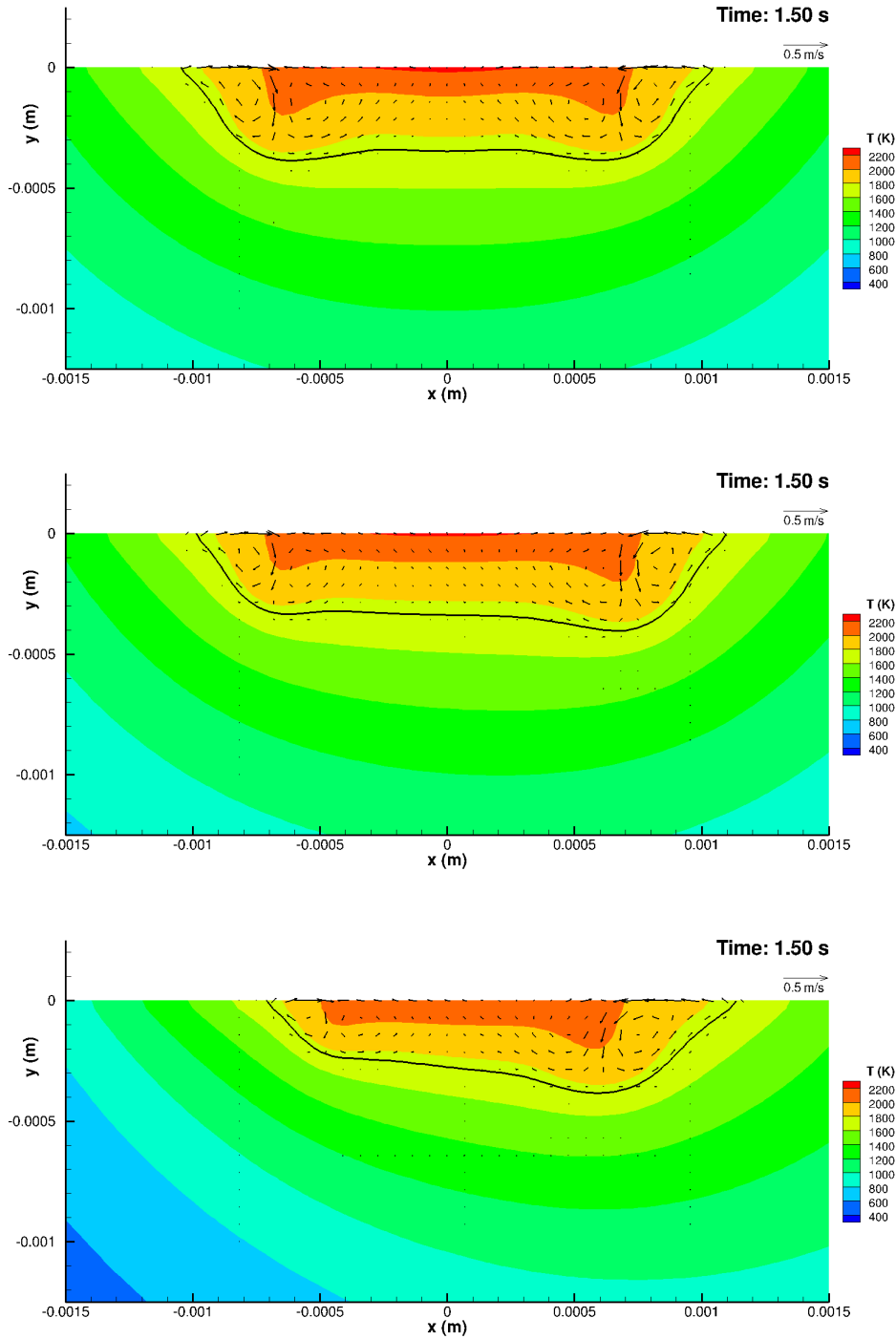


Figure 4.13: The side views of the weld pools of three cases with a sign changing $d\sigma/dT$

Case	$U_{t,x}$	$d\sigma/dT$	Computational Domain	# Cells
3.1	0 mms^{-1}	+/-	20 x 20 x 10 mm	104 x 80 x 40
3.2	1 mms^{-1}	+/-	20 x 20 x 10 mm	116 x 80 x 40
3.3	5 mms^{-1}	+/-	22 x 20 x 10 mm	128 x 80 x 40

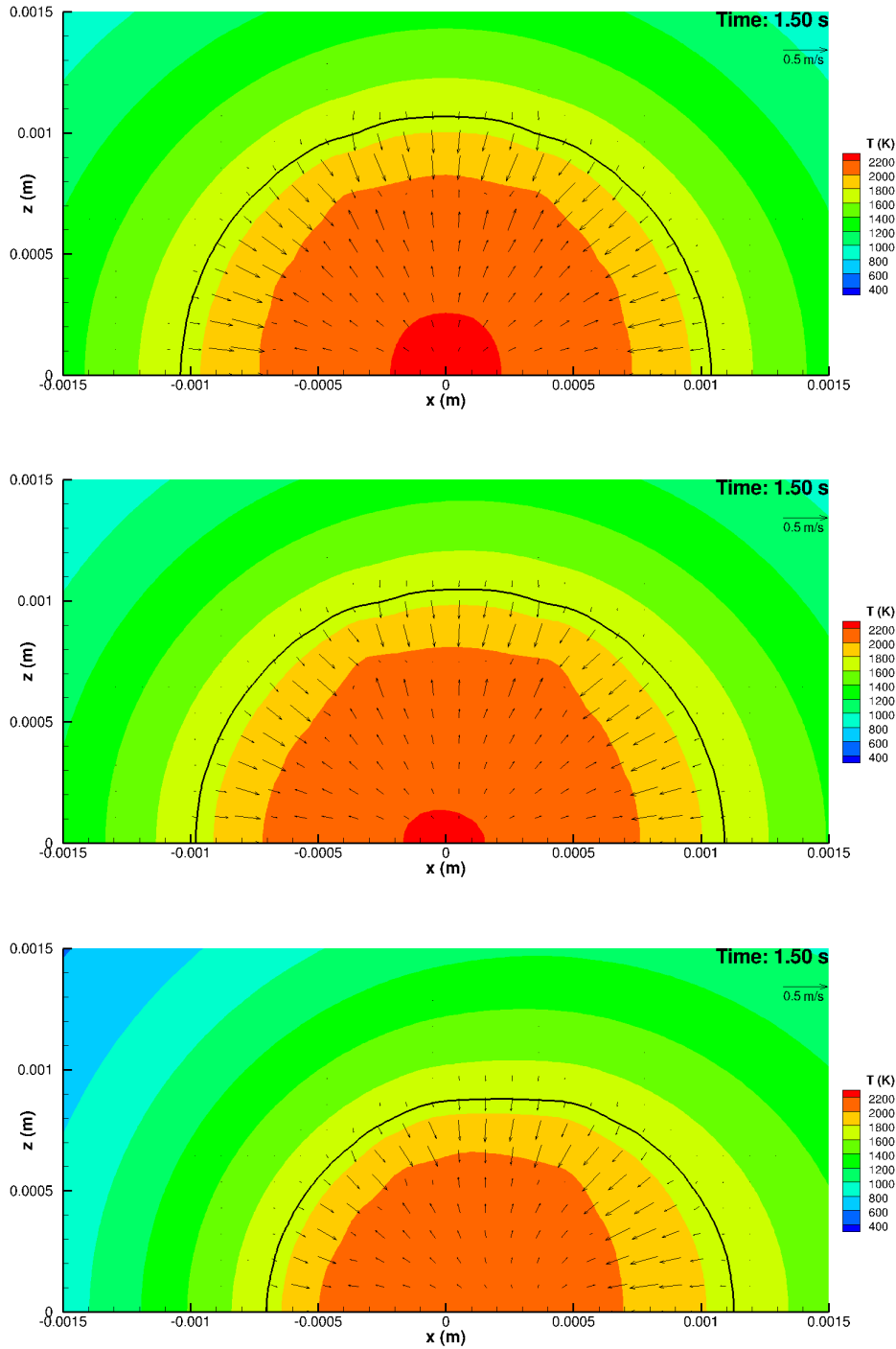


Figure 4.14: The top views of the weld pools of three cases with a sign changing $d\sigma/dT$

5 Closure

5.1 General conclusions

The two major goals of this work included the theoretical derivation of the governing equations for heat transfer, phase change and fluid flow in welding with a heat source moving with constant velocity and the implementations of these equations in an existing OpenFOAM solver.

To achieve the first goal, theoretical derivations of the continuity, heat and momentum equations in spot welding for the stationary frame of reference have been done in chapter 2. Special attention was given to the modeling of the phase change, the fluid flow in the mushy zone and the modeling of the surface forces due to the Marangoni effect. In section 2.4 these findings are transformed to a reference frame attached to moving heat source using $\vec{V} = \vec{U} + \vec{U}_t$ resulting in equations 2.30, 2.31 and 2.32 which are the governing equations for mass, heat and momentum transfer in welding with a moving heat source.

To achieve the second goal, the new governing equations were implemented in an existing OpenFOAM solver and benchmarked in three steps. In section 4.1 analytical solutions for thermal conduction were successfully compared with simulation results. In section 4.2 both the modified and the original solver were used for the simulation of a stationary and a moving heat source case, they achieved identical results with the modified solver having a 12.5% lower execution-time. For simulation with higher welding velocities or longer simulation times the decrease in clock-time will be larger. Finally in section 4.3 nine welding cases with different heat source velocities and / or surface tension coefficients were discussed.

To summarize the conclusions:

- The governing equation for welding with a moving heat source were derived and can be found in section 2.4.
- These equations have been implemented in an existing OpenFOAM solver which is benchmarked successfully in chapter 4.

5.2 Recommendations for future work

5.2.1 Free surface deformation

All results generated in this work incorporate the assumption of no surface deformations during the welding process. From experiments we know the weld pool surface can expe-

rience deformations when the surface tension forces can not balance the viscous forces. The extent to which this can happen is characterized by the Capillary number:

$$Ca = \frac{\mu U}{\sigma_0}$$

In our simulations the Capillary number is in the order of 10^{-1} , which is sufficiently large for surface deformations to occur and to influence the fluid flow within the weld pool[15]. Allowing weld pool surface deformation is therefore more realistic and desirable.

When implementing free surface deformation special attention has to be given to the heat transfer through the weld pool surface and the modeling of the Marangoni forces. In this work these two are applied as boundary conditions but for free surface deformation they have to be implemented as source terms in the heat and momentum equation.

5.2.2 Mesh refinement

The number of computational cells used during fluid flow simulations in this thesis is in the order of $10^5 - 10^6$, decreasing the amount of cells leads to a large decrease in the computational load. There are multiple options to achieve this decrease; 2D-modeling, optimizing the mesh using the knowledge gained in this work, and adaptive mesh refinement.

The first option is 2D-modeling instead of 3D modeling which can be used in benchmarking new features implemented in the solver. For most situations this leads to sufficient results for initial testing.

The second option is improving the mesh used in this work taking into account the results simulated in section 4.3, since only mesh refinement is required where the gradients are large, i.e. in the weld pool area. Comparing these results with the mesh shown in figure 3.1 we can conclude that progress can be made in coarsening the mesh towards the boundaries and along the symmetry axis.

The third option is adaptive mesh refinement where you start the simulation on a coarse mesh and adapt the refinement of the mesh when gradients exceed a certain threshold. In this method the computational mesh is always optimized but the adaptive refinement procedure introduces a large computational overhead which also has to be taken into account.

5.2.3 Investigation of the symmetry breaking cases

In section 4.3 we found that for the welding cases with a stationary heat source the expected symmetry of the weld pool was broken. The symmetry breaking may be of physical or numerical origin and therefore has to be investigated. This can be done experimentally by looking at the symmetry of solidified weld pool samples or numerically by high fidelity simulations to rule out numerical instabilities.

Bibliography

- [1] Openfoam - the opensource cfd toolbox: Openfoam programmer's guide. Technical report, OpenCFD Ltd., February 2014.
- [2] R.B. Bird, W.E. Stewart, and E.N. Lightfoot. *Transport Phenomena*. Wiley International edition. Wiley, 2007.
- [3] Suman Chakraborty and Pradip Dutta. Numerical modeling of heat and mass transfer in laser surface alloying: Non-equilibrium solidification effects. *Materials and Manufacturing Processes*, 17(4):455–468, 2002.
- [4] S. A. David and T. DebRoy. Current issues and problems in welding science. *Science*, 257(5069):497–502, 1992.
- [5] C.J. Hoogendoorn. *Fysische Transportverschijnselen II*. Delftse Uitgevers Maatschappij b.v., 1985.
- [6] R.I Issa. Solution of the implicitly discretised fluid flow equations by operator-splitting. *Journal of Computational Physics*, 62(1):40 – 65, 1986.
- [7] H. Jasak. *Error Analysis and Estimation for the Finite Volume Method with Applications to Fluid Flows*. PhD thesis, Imperial College of Science, Technology and Medicine, June 1996.
- [8] A. Kidess. Mintweld deliverable D4.2.1 - Validated CFD model for hydrodynamics and mixing in laser welding. Technical report, Department of Transport Phenomena, Delft University of Technology, December 2012.
- [9] C.S. Kim. Thermophysical properties of stainless steels. Technical report, Sep 1975.
- [10] K. Mundra, T. DebRoy, and K. M. Kelkar2. Numerical prediction of fluid flow and heat transfer in welding with a moving heat source. *Numerical Heat Transfer, Part A: Applications*, 29(2):115–129, 1996.
- [11] W. Pitscheneder, T. DebRoy, K. Mundra, and R. Ebner. Role of sulfur and processing variables on the temporal evolution of weld pool geometry during multikilowatt laser beam welding of steels. *WELDING JOURNAL*, 75(3), March 1996.
- [12] W. Pitscheneder, R. Ebner, T. Hong, T. Debroy, K. Mundra, and R. Benes. Experimental and numerical investigation of transport phenomena in conduction mode weld pools. In H. Cerjak and H. K. D. H. Bhadeshia, editors, *Mathematical Modelling of Weld Phenomena 4*, Materials Modelling Series, pages 3–25, London, 1997. The Institute of Materials, IOM Communications.

- [13] P Sahoo, T DebRoy, and MJ McNallan. Surface tension of binary metal - surface active solute systems under conditions relevant to welding metallurgy. *Metallurgical Transactions B*, 19(3):483–491, 1988.
- [14] Zaki Saldi, Anton Kidess, Sasa Kenjeres, Chris Kleijn, Chuangxin Zhao, and Ian Richardson. Marangoni driven free surface microflows in liquid metal weld pools. In Stéphane Colin and Gian L. Morini, editors, *2nd European Conference on Microfluidics*. Société Hydrotechnique de France, SHF, 2010.
- [15] Zaki S. Saldi. *Marangoni Driven Free Surface Flows in Liquid Weld Pools*. PhD thesis, Delft University of Technology, 2012.
- [16] M. Tong, J. Liu, Y. Xie, HB Dong, RL Davidchack, J. Dantzig, D. Ceresoli, N. Marzari, A. Cocks, C. Zhao, I. Richardson, A. Kidess, C. Kleijn, L. Hoglund, S. W. Wen, R. Barnett, and D. J. Browne. An integrated framework for multi-scale multi-physics numerical modelling of interface evolution in welding. In *IOP Conference Series: Materials Science and Engineering*, volume 33, pages 12029–12040. IOP Publishing, 2012.
- [17] Mingming Tong, Gregory Duggan, Jun Liu, Yu Xie, Mike Dodge, Lee Aucott, Hongbiao Dong, Ruslan L. Davidchack, Jon Dantzig, Olga Barrera, Alan C. F. Cocks, Hiroto Kitaguchi, Sergio Lozano-Perez, Chuangxin Zhao, Ian Richardson, Anton Kidess, Chris R. Kleijn, Shuwen Wen, Roger Barnett, and David J. Browne. Multi-scale, multiphysics numerical modeling of fusion welding with experimental characterization and validation. *Jom*, 65(1):99–106, 2013.
- [18] V. R. Voller and C. R. Swaminathan. Eral source-based method for solidification phase change. *Numerical Heat Transfer, Part B: Fundamentals*, 19(2):175–189, 1991.
- [19] V. R. Voller, C. R. Swaminathan, and B. G. Thomas. Fixed grid techniques for phase change problems: A review. *International Journal for Numerical Methods in Engineering*, 30(4):875–898, 1990.
- [20] C. Winkler, G. Amberg, H. Inoue, and T. Koseki. A numerical and experimental investigation of qualitatively different weld pool shapes. In H. Cerjak and H. K. D. H. Bhadeshia, editors, *Mathematical Modelling of Weld Phenomena 4*, Materials Modelling Series, pages 37–69, London, September 1997. IOM Communications Ltd.
- [21] C. X. Zhao, C. Kwakernaak, Y. Pan, I. M. Richardson, Z. Saldi, S. Kenjeres, and C. R. Kleijn. The effect of oxygen on transitional Marangoni flow in laser spot welding. *Acta Materialia*, 58(19):6345–6357, November 2010.
- [22] Chuangxin Zhao, Ian M. Richardson, Chris Kleijn, Sasa Kenjeres, and Zaki Saldi. A stereo vision visualization method in welding. In TE Simos, G Psihoyios, and C Tsitouras, editors, *Numerical Analysis and Applied Mathematics*, volume 1048 of *AIP CONFERENCE PROCEEDINGS*, pages 617–620. Greek Minist Educ & Religious Affairs; European Soc Computat Methods Sci & Engn, 2008.

6 Appendix

6.1 Derivations for the change of reference frame

6.1.1 Continuity equation

In the moving reference frame we decompose the net velocity into a convective part and a part due to the heat source velocity.

$$\vec{V} = \vec{U} + \vec{U}_t \quad (6.1)$$

We insert this net velocity into the continuity equation 2.23

$$\frac{\partial}{\partial t} \rho + \nabla \cdot (\rho \vec{V}) = 0 \quad (6.2)$$

$$\frac{\partial}{\partial t} \rho + \nabla \cdot (\rho(\vec{U} + \vec{U}_t)) = 0 \quad (6.3)$$

$$\frac{\partial}{\partial t} \rho + \nabla \cdot (\rho \vec{U}) + \nabla \cdot (\rho \vec{U}_t) = 0 \quad (6.4)$$

Using the fact that the heat source velocity is constant, we end up with:

$$\frac{\partial}{\partial t} \rho + \nabla \cdot (\rho \vec{U}) = 0 \quad (6.5)$$

6.1.2 Heat equation

We first combine equation 2.7 from section 2.2.1 with equation 2.12 from section 2.2.2 to obtain the full heat equation.

$$\frac{\partial H}{\partial t} + \nabla \cdot (H \vec{U}) = (\nabla \cdot \lambda \nabla T) \quad (6.6)$$

$$\rho c_p \frac{\partial T}{\partial t} + \rho L \frac{\partial g}{\partial t} + \nabla \cdot (\rho(c_p T + gL) \vec{U}) = (\nabla \cdot \lambda \nabla T) \quad (6.7)$$

Similar to the previous section , we insert the velocity \vec{V} .

$$\rho c_p \frac{\partial T}{\partial t} + \rho L \frac{\partial g}{\partial t} + \nabla \cdot (\rho(c_p T + gL) \vec{V}) = (\nabla \cdot \lambda \nabla T) \quad (6.8)$$

$$\rho c_p \frac{\partial T}{\partial t} + \rho L \frac{\partial g}{\partial t} + \nabla \cdot (\rho(c_p T + gL)(\vec{U} + \vec{U}_t)) = (\nabla \cdot \lambda \nabla T) \quad (6.9)$$

$$\rho c_p \frac{\partial T}{\partial t} + \rho L \frac{\partial g}{\partial t} + \nabla \cdot (\rho(c_p T + gL)\vec{U}) + \nabla \cdot (\rho(c_p T + gL)\vec{U}_t) = (\nabla \cdot \lambda \nabla T) \quad (6.10)$$

$$\rho c_p \frac{\partial T}{\partial t} + \rho L \frac{\partial g}{\partial t} + \nabla \cdot (\rho c_p T \vec{U}) + \nabla \cdot (\rho g L \vec{U}) + \nabla \cdot (\rho c_p T \vec{U}_t) + \nabla \cdot (\rho g L \vec{U}_t) = (\nabla \cdot \lambda \nabla T) \quad (6.11)$$

Because the relative velocity between the solid and liquid phase is zero, the term $\nabla \cdot (\rho g L \vec{U}_t)$, is set to zero. leading to the governing equation for the heat transport in the workpiece.

$$\rho c_p \frac{\partial T}{\partial t} + \rho L \frac{\partial g}{\partial t} + \nabla \cdot (\rho c_p T \vec{U}) + \nabla \cdot (\rho c_p T \vec{U}_t) + \nabla \cdot (\rho g L \vec{U}) = (\nabla \cdot \lambda \nabla T) \quad (6.12)$$

6.1.3 Momentum equation

In section 2.3.1 we found the momentum equation in the stationary frame of reference to be

$$\frac{\partial}{\partial t} \rho \vec{U} + \nabla \cdot (\rho \vec{U} \vec{U}) + \nabla \cdot (\mu \nabla \vec{U}) = -C \frac{(1-g)^2}{g^3 + \epsilon} \vec{U} - \rho \vec{g} - \nabla p \quad (6.13)$$

Substituting the velocity \vec{V} in this formula results in:

$$\frac{\partial}{\partial t} \rho \vec{V} + \nabla \cdot (\rho \vec{V} \vec{V}) + \nabla \cdot (\mu \nabla \vec{V}) = -C \frac{(1-g)^2}{g^3 + \epsilon} \vec{V} - \rho \vec{g} - \nabla p \quad (6.14)$$

the time derivative term on the left hand side is simplified as follows:

$$\frac{\partial}{\partial t} \rho \vec{V} = \frac{\partial}{\partial t} \rho (\vec{U} + \vec{U}_t) = \frac{\partial}{\partial t} \rho \vec{U} + \frac{\partial}{\partial t} \rho \vec{U}_t = \frac{\partial}{\partial t} \rho \vec{U} \quad (6.15)$$

For the convective term we have

$$\nabla \cdot (\rho \vec{V} \vec{V}) = \nabla \cdot (\rho \vec{U} \vec{U}) + \nabla \cdot (\rho \vec{U}_t \vec{U}) + \nabla \cdot (\rho \vec{U} \vec{U}_t) + \nabla \cdot (\rho \vec{U}_t \vec{U}_t) \quad (6.16)$$

Since the welding velocity is constant, the last two terms are zero.

The diffusive term is can be simplified as:

$$\nabla \cdot (\mu \nabla \vec{V}) = \nabla \cdot (\mu \nabla (\vec{U} + \vec{U}_t)) = \nabla \cdot (\mu \nabla \vec{U}) + \nabla \cdot (\mu \nabla \vec{U}_t) \quad (6.17)$$

Assuming constant viscosity and taking into account that derivatives of the welding velocity are zero leaves us with.

$$\nabla \cdot (\mu \nabla \vec{U}) = \mu \nabla^2 \vec{U} \quad (6.18)$$

Since the mushy zone dampening source term incorporates the velocity too, we are tempted to substitute the velocity \vec{V} in this term which would result in.

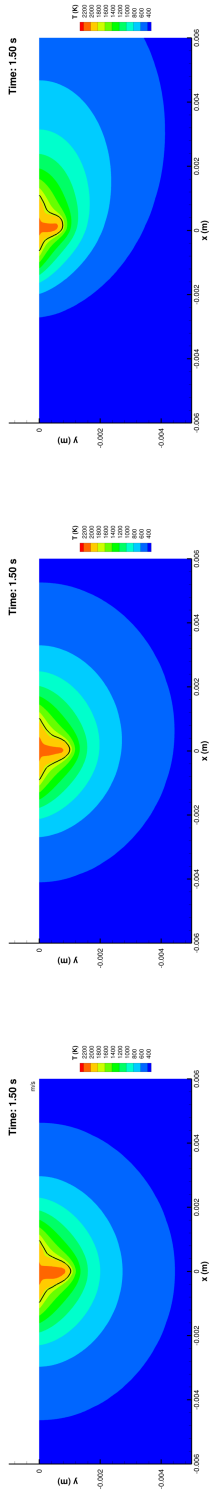
$$\vec{F}_{damp} = -C \frac{(1-g)^2}{g^3 + \epsilon} \vec{V} = -C \frac{(1-g)^2}{g^3 + \epsilon} (\vec{U} + \vec{U}_t) = -C \frac{(1-g)^2}{g^3 + \epsilon} \vec{U} + -C \frac{(1-g)^2}{g^3 + \epsilon} \vec{U}_t \quad (6.19)$$

Because the relative velocity between the solid and liquid phase is zero, the term $-C \frac{(1-g)^2}{g^3 + \epsilon} \vec{U}_t$, is set to zero.

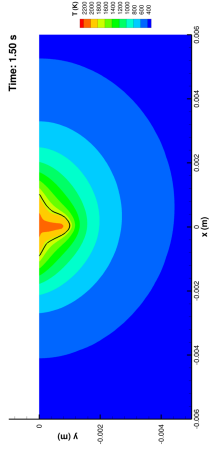
Combining the separated terms again results in the modified momentum equation:

$$\frac{\partial}{\partial t} \rho \vec{U} + \nabla \cdot (\rho \vec{U} \vec{U}) + \nabla \cdot (\rho \vec{U}_t \vec{U}) + \mu \nabla^2 \vec{U} = -C \frac{(1-g)^2}{g^3 + \epsilon} \vec{U} - \rho \vec{g} - \nabla p \quad (6.20)$$

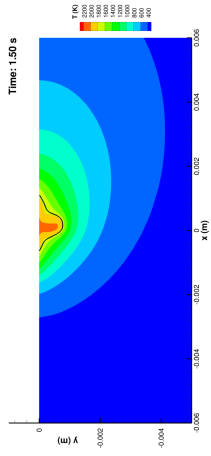
6.1.4 Overview of the validation cases of subsection 4.3



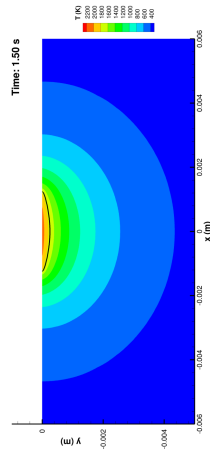
(a) $U_t = 0 \text{ mms}^{-1}$



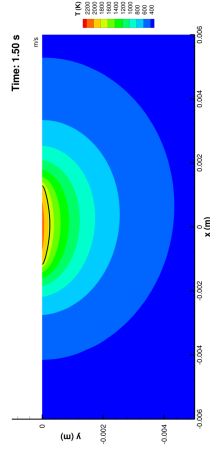
(b) $U_t = 1 \text{ mms}^{-1}$



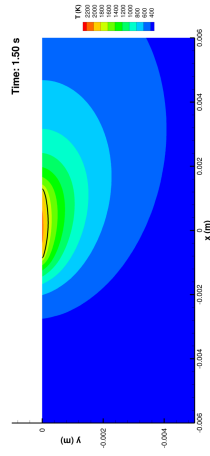
(c) $U_t = 5 \text{ mms}^{-1}$



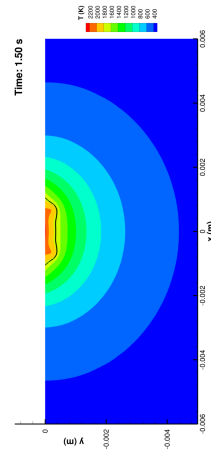
(d) $U_t = 0 \text{ mms}^{-1}$



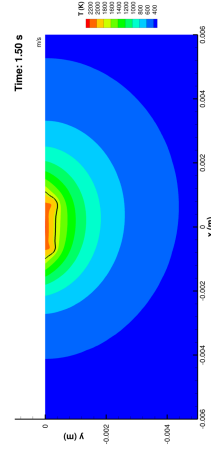
(e) $U_t = 1 \text{ mms}^{-1}$



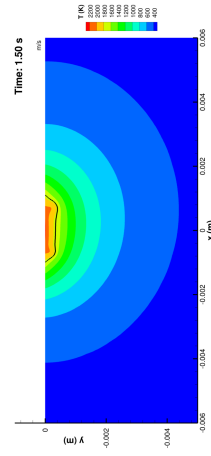
(f) $U_t = 5 \text{ mms}^{-1}$



(g) $U_t = 0 \text{ mms}^{-1}$



(h) $U_t = 1 \text{ mms}^{-1}$



(i) $U_t = 5 \text{ mms}^{-1}$

Figure 6.1: Overview of the temperature profile side views shown in section 4.3. The surface tensions coefficients for the top, middle and bottom row are respectively positive, negative and sign changing.

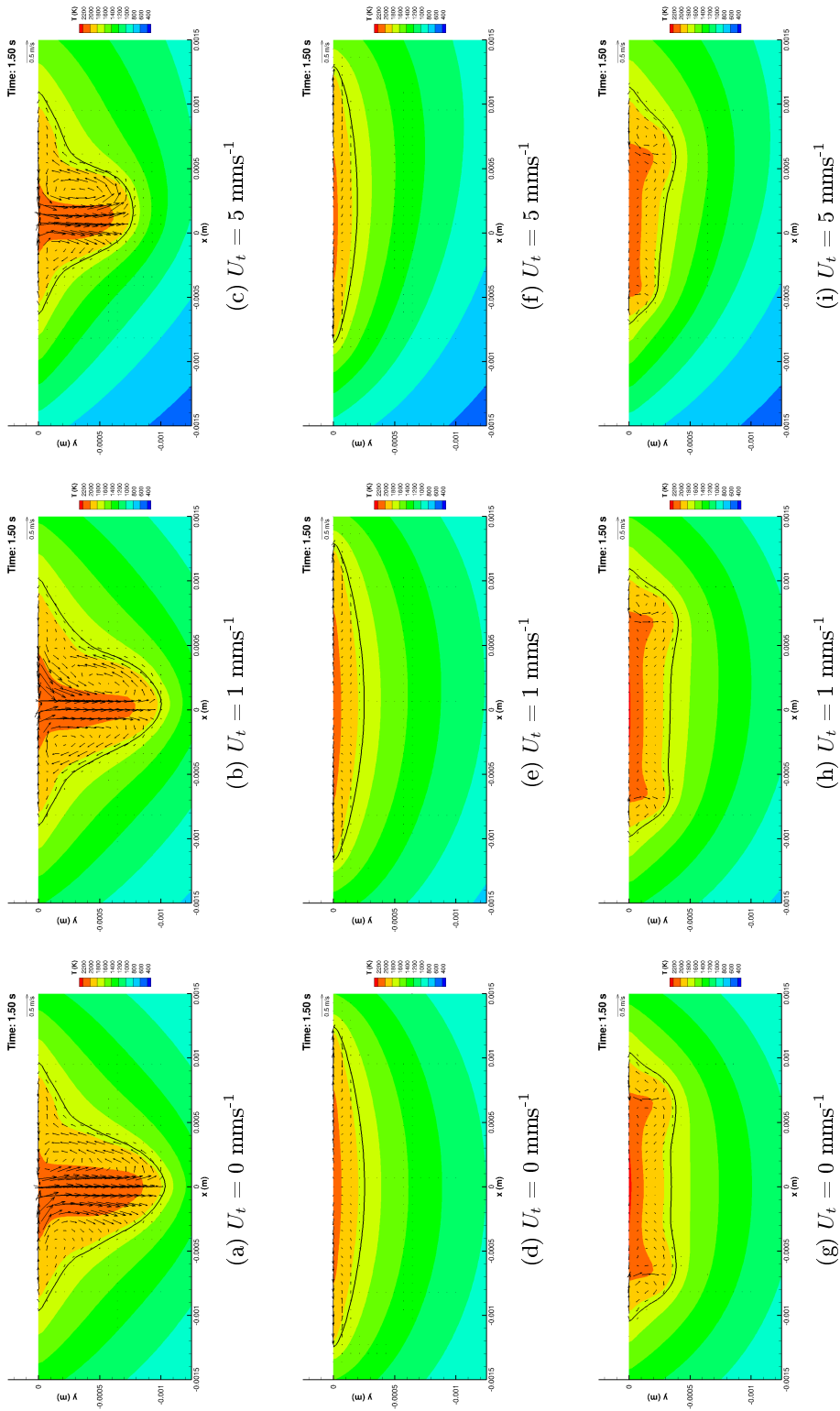


Figure 6.2: Overview of the weld pool side views in section 4.3. The surface tensions coefficients for the top, middle and bottom row are respectively positive, negative and sign changing.

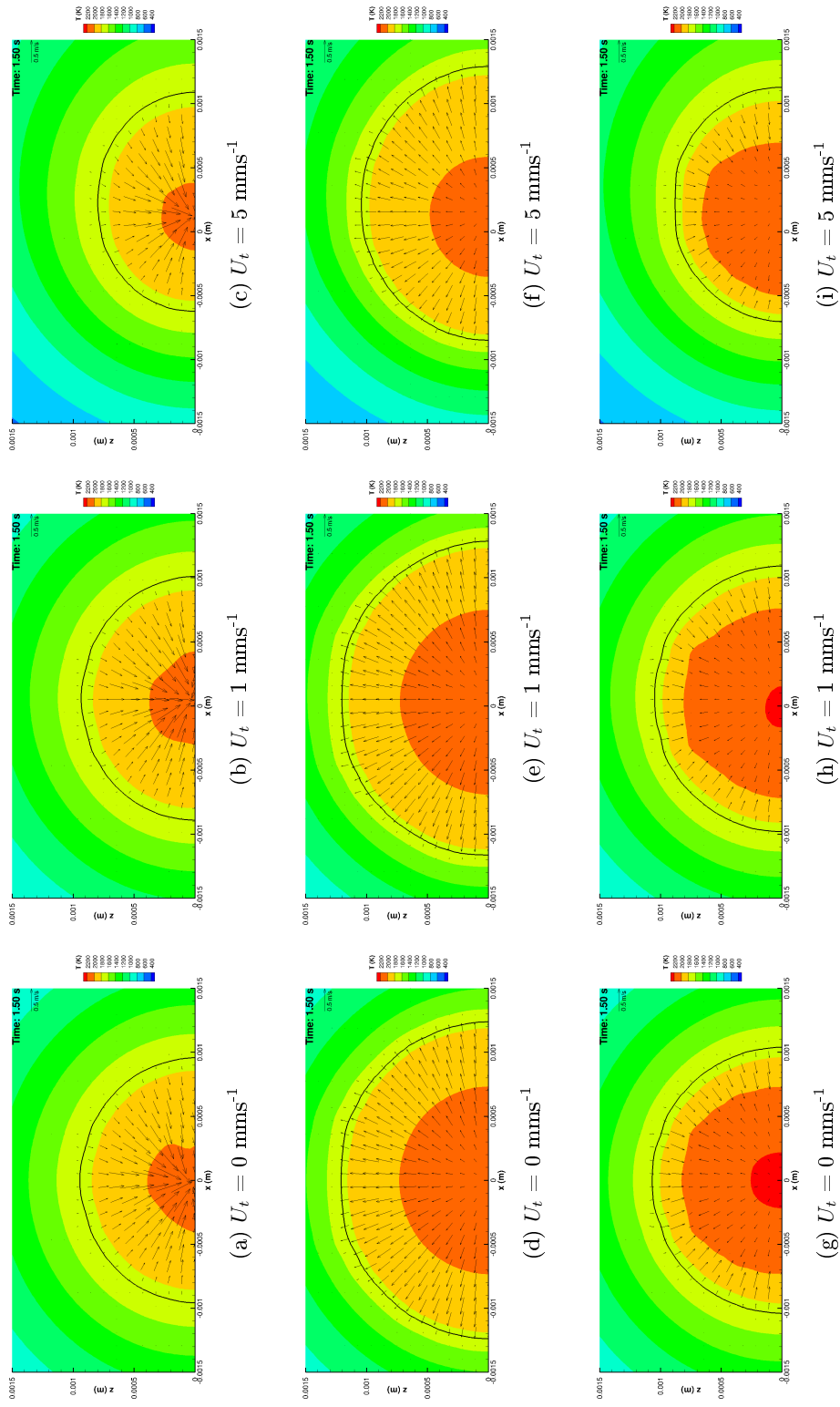


Figure 6.3: Overview of the weld pool top views shown in section 4.3. The surface tensions coefficients for the top, middle and bottom row are respectively positive, negative and sign changing.